A new seismic tomography of Aigion area (Gulf of Corinth, Greece) from the 1991 data set

D. Latorre,[1] J. Virieux,[1] T. Monfret,[1] V. Monteiller,[2] T. Vanorio,[1] J.-L. Got[2] and H. Lyon-Caen[3]

[1] *UMR Géosciences Azur, Valbonne, France. E-mail: latorre@geoazur.unice.fr*
[2] *Laboratoire de Géophysique Interne et Tectonophysique, Université de Savoie, Le Bourget-du-Lac, France*
[3] *Laboratoire de géologie, École normale supérieur, Paris, France*

SUMMARY

A new three-dimensional delay traveltime tomography is performed to image the intermediate structure of the western Gulf of Corinth. A large data set, collected in 1991 during a two-month passive tomographic experiment, has been reanalysed for the reconstruction of detailed Vp and Vs images. An improved tomography method, based on an accurate traveltime computation, is applied to invert simultaneously delayed P and S first-arrival traveltimes for both velocity and hypocentre parameters. We perform different synthetic tests to analyse the sensitivity of tomography results to the model parametrization and to the starting 1-D model selection. The analysis of the retrieved Vp and Vs models as well as deduced Vp/Vs and $Vp \cdot Vs$ images allows us to interpret and delineate the distribution of lithological variation, porosity/crack content and fluid saturation in the upper 9–11 km of the crust beneath the gulf. The tomographic models image a rather complex crustal structure, which is characterized by a vertical change in both velocity features and seismicity distribution. We identify a shallower zone of the crust (0–5 km depth), in which velocity distributions seem to be controlled by the still active N–S extensional regime and a deeper zone (7–11 km depth), which matches the seismogenic zone. The correlation between this latter and a specific unit of the Hellenic mountain structure (the Pyllite–Quartzite series) allows us to suggest a possible explanation for seismicity concentration in a narrow band at 7–9 km depth. Finally, the occurrence of clusters showing low-angle normal fault mechanisms in areas characterized by high Vp/Vs values indicates a possible role of fluids in triggering brittle creep along the identified low-angle normal faults.

Key words: Gulf of Corinth, low-angle detachment, seismic tomography, Vp/Vs, $Vp \cdot Vs$.

1 INTRODUCTION

During the last 15 yr, numerous multidisciplinary studies have been carried out to understand the tectonic evolution of the Gulf of Corinth as well as the mechanisms related to the seismicity in this area (e.g. Rigo *et al.* 1996; Bernard *et al.* 1997; Briole *et al.* 2000; Moretti *et al.* 2003). The high interest for this active continental rift arises from the high extension rate of 1–1.4 cm yr^{-1} (Briole *et al.* 2000) coupled to an intense and continuous seismic activity showing peculiar characteristics (Rigo *et al.* 1996; Bernard *et al.* 1997; Hatzfeld *et al.* 2000; Lyon-Caen *et al.* 2004). So far, although many tectonic models have been proposed, the knowledge of the crustal structure is such that the relationship between seismic activity at depth and the major faults is still debated (Doutsos & Poulimenos 1992; Ori 1989; Hatzfeld *et al.* 2000; Sorel 2000; Jolivet 2001, among others). Therefore, a comprehensive knowledge of the crustal structure constitutes an essential step to understand the tectonic evolution of the Corinth rift.

In 1991, a seismological experiment was carried out in the western Gulf of Corinth. Part of the recorded data set was analysed by Le Meur *et al.* (1997) who have performed the first tomographic study of this area. The main result of this study was the interpretation of P velocity anomalies as important structural variations occurring at depth. However, although this earlier study represents the first attempt to show the crustal image of the western Gulf of Corinth, the model interpretation suffered from a limited resolution of tomographic results as well as from the lack of a reliable analysis of relations between P and S velocity variations.

Later on, the multidisciplinary study concerning the 1995 Aigion earthquake and its aftershocks (Bernard *et al.* 1997) has pointed out that either high-pressured fluids or stress rotations coming from crustal heterogeneities might have played a role in triggering the Aigion earthquake as well as other moderate earthquakes in the northern part of the gulf. A new tomographic study may bring new constraints in these interpretations. Indeed, fluid content and

GJI Seismology

porosity/crack distribution can be detected by interpreting spatial variations of parameters as Vp/Vs ratio and $Vp \cdot Vs$ product.

A review of present knowledge about relationships between Vp/Vs ratio and rock physical properties has been provided by Sanders *et al.* (1995). Also, Iverson *et al.* (1989) have suggested the use of $Vp \cdot Vs$ product as a tool in the detection of porosity variation in seismic interpretation. Successively, other authors have used these parameters in tomography studies (Lees & Wu 2000; Monna *et al.* 2003). In particular, Lees & Wu (2000) have carefully discussed the capability of $Vp \cdot Vs$ analysis for interpreting spatial crack distribution at crustal scale. Similarly, Zhao *et al.* (1996) and Thurber *et al.* (1997) have underlined the relation between the Vp/Vs parameter and variations of rock physical properties in seismogenic areas.

An improved tomographic technique applied to the updated 1991 database has allowed us to obtain seismic images of the Corinth rift structure with higher resolution power compared with the previous tomographic study (Le Meur *et al.* 1997). Also, the reconstructed Vp/Vs and $Vp \cdot Vs$ images have provided new insights on the crustal structures at depth through a relative estimate of the physical properties affecting rock seismic velocities.

In the framework of the continuous efforts aimed to understand the tectonic evolution of this area, this paper presents new reliable seismic tomographic images that bring further key elements for future geodynamic modelings.

2 GEOLOGICAL FRAMEWORK

The Gulf of Corinth is bounded by continental Greece to the north and northern Peloponnesus to the south (Fig. 1). The coast shape defines an approximately 120°N-oriented structure 130 km long, which is wider and deeper on the eastern side near the town of Corinth, while it is narrow and shallower on the western side near Psatophyrgos. Many authors consider the Gulf of Corinth as an asymmetric half-graben having major north-dipping normal faults located on its southern border and minor antithetic south-dipping faults on the northern border (e.g. Ori 1989; Doutsos & Poulimenos 1992; Armijo *et al.* 1996; Sorel 2000). The major north-dipping faults are organized in a right-stepping *en échelon* system and show a strike that ranges between W–E and WNW–ESE with a dip of 55°–70° northward (Armijo *et al.* 1996). The northern part of the gulf does not show evidence of synrift sediments (Ori 1989; Doutsos & Poulimenos 1992). On the contrary, very thick (∼1 km) synrift deposits (Doutsos & Poulimenos 1992; Flotté & Sorel 2001) crop out in north Peloponnesus, which is subject to a rapid uplift (e.g. Armijo *et al.* 1996).

Two different tectonic phases seem to be responsible for the extreme complexity of the lithospheric structure in the Corinth region. The first one is represented by the Cenozoic E–W compressional phase, which gave rise to the crustal thickening and the NNW–SSE-trending fabric of the Hellenic orogenic belt (Aubouin *et al.* 1962; Jacobshagen *et al.* 1978). The Hellenic mountains are essentially composed of a stack of Mesozoic tectonic units. In the western Gulf of Corinth, the Pindos series represents the shallowest unit. It mainly consists of deep water carbonates having a minimum thickness of 3500 m (Aubouin *et al.* 1962; Pham *et al.* 2000) and cropping out both on the continental Greece and on Peloponnesus. This unit overthrusted the Gavrovo–Tripolitza unit, a 2–3 km thick series of carbonate platform sediments, which crop out to the west on the both sides of the gulf (Doutsos & Poulimenos 1992; Dornsiepen *et al.*
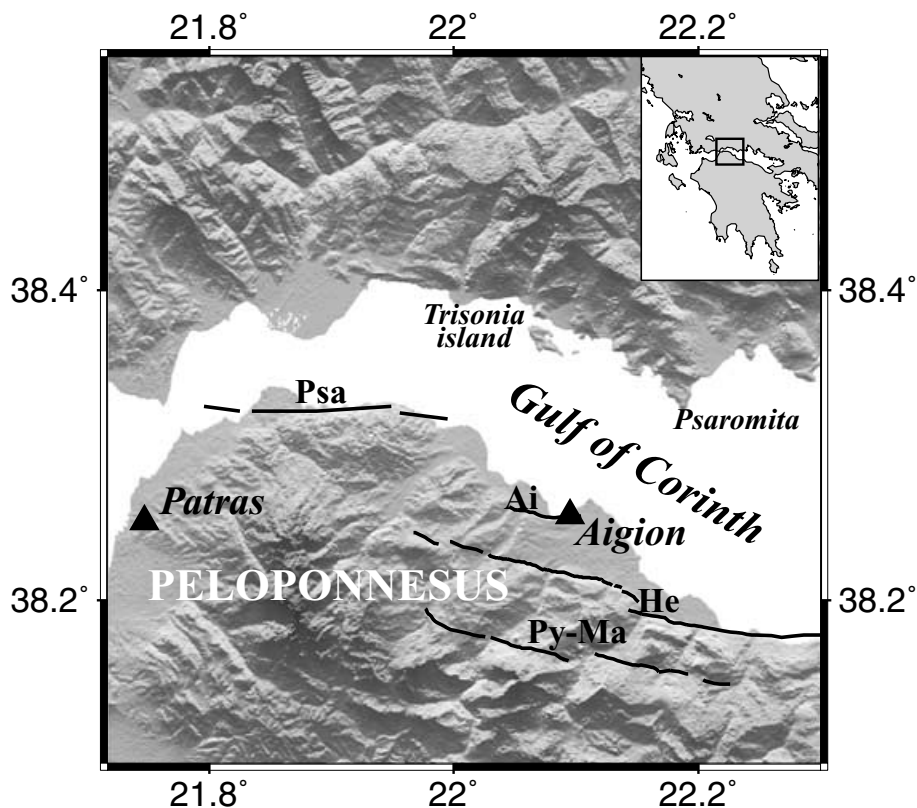

Figure 1. Map of the western Gulf of Corinth. The location of the selected area is indicated on the right corner of the figure. The major north-dipping normal faults cropping out in the Peloponnesus are represented by dark lines. Psathopyrgos fault (Psa), Aigion fault (Ai), Helike fault (He), Pyrgaki–Mamoussia fault (Py–Ma).

2001). Beneath the Tripolitza unit, many authors (Jacobshagen *et al.* 1978; Dornsiepen *et al.* 2001) suggest the presence of the Phyllite–Quartzite series whose estimated thickness is approximately 1.5–2 km (Jacobshagen *et al.* 1978; Doutsos & Poulimenos 1992). The Phyllite–Quartzite series crops out in a tectonic window located on the south of the studied area, whereas its extension towards the continental Greece is still being debated. This particular series differs from the upper ones because of both its tectonometamorphic origin and lithology, which shows to be characterized by an alternation of phyllites, schists and quartzites (Dornsiepen *et al.* 2001).

The second tectonic phase is represented by the extension of the Aegean region, which started in Miocene time (Le Pichon *et al.* 1995). This extensional phase was initially characterized by a predominant NE–SW direction in the the Corinth region (e.g. Mercier *et al.* 1987; Jolivet & Patriat 1999). Many authors (Ori 1989; Armijo *et al.* 1996) postulated that a proto-Corinth rift was forming during this phase when periodic NW–SE-trending crustal instabilities took place (Tiberi *et al.* 2001). During the Quaternary, the Aegean extension was accelerated by the southwestward propagation of the North Anatolian fault (NAF), which has reactivated the structure of the Corinth rift approximately 1 Ma (Armijo *et al.* 1996). Presently, the rift extension is accommodated in a narrow band off-shore presenting an extension rate that is greater in the western part (16 mm yr^{-1} 185°NE at Aigion) compared with the eastern part (11 mm yr^{-1} 185°NE at Xilocastro; Avallone *et al.* 2004).

A peculiar characteristic of the western Gulf of Corinth is the background microseismic activity, which appears very intense and concentrated in a narrow band at 6–10 km depth and is distributed along a trend dipping approximately 15° northwards (Rigo *et al.* 1996). Rigo *et al.* (1996) have postulated that this microseismicity is related to either a low-angle active fault or a low-angle detachment zone lying at 9–11 km depth. In this model, Rigo *et al.* (1996) suggest that microseismicity mainly occurs at the intersection between the major steeper normal faults that crop out in the southern part of the gulf and the low-angle north-dipping detachment zone. The extension of major steep north-dipping faults down to 8–12 km depth was also hypothesized by Doutsos & Poulimenos (1992), following the model suggested by King *et al.* (1985) for the eastern Gulf of Corinth. On the contrary, Sorel (2000) proposes a model in which an active low-angle detachment fault (the Kelmos fault) represents the major extensional structure of the rift, whereas the other steeper normal faults cropping out on the Peloponnesus are only secondary listric structures, which branch the master fault at a relative shallow depth. The presence of active low-angle normal faults beneath the gulf has been confirmed by both cluster analysis of microearthquakes (Rietbrock *et al.* 1996) and aftershock studies of large events, such as those from the Galaxidi earthquake (Hatzfeld *et al.* 1996) and the Aigion earthquake (Bernard *et al.* 1997). However, in the rotating domino model proposed by Hatzfeld *et al.* (2000), the seismicity occurring at 8–12 km is not associated to a subhorizontal active detachment, but to a rise of the brittle–ductile transition resulting from the rapid extension rate of the western Corinth rift.

In the view of the points made above, it is clear that this clash of opinions still calls into question the structural framework of the Gulf of Corinth. Here is the need of 3-D velocity images and seismicity distribution, as presented in this paper.

3 PROBLEM FORMULATION

In order to obtain a three-dimensional seismic velocity image of the Aigion area, delayed *P* and *S* first-arrival times are simultaneously inverted for both earthquake locations and velocity distribution. The simultaneous inversion of these different classes of parameters has been extensively discussed by Thurber (1992) as a solution of the hypocentre–velocity structure coupling problem in local earthquake tomography. In order to solve the inverse problem related to the nonlinear relation between traveltimes on the one hand and velocity and hypocentre parameters on the other, we follow an iterative scheme by which a linearized delay traveltime inversion is performed (Aki & Lee 1976; Spakman & Nolet 1988; Hole 1992; Benz *et al.* 1996; Le Meur *et al.* 1997, among others). At each iteration, wave fronts of first-arrival times are calculated in the whole medium by using the Podvin and Lecomte algorithm that is based on a finite difference solution of the eikonal equation (Podvin & Lecomte 1991). Both *P* and *S* velocity models are parametrized by a three-dimensional, regularly spaced, rectangular grid, which constitutes the inversion grid.

The estimate of first-arrival traveltimes by the Podvin and Lecomte algorithm requires a finer grid of cubic cells as the technique assumes constant slowness in each cell. These slownesses are deduced by trilinear interpolation of the inversion grid. For each station, the solution of the eikonal equation provides a first estimation of traveltimes at each node of the finer grid. By following the gradient of the estimated traveltimes, we are able to trace the ray back from the event to the receiver. After this *a posteriori* ray tracing, the finer grid is destroyed and is no longer used.

Once rays are computed for each event–receiver pair, more precise traveltimes are recalculated by performing a numerical integration of the slowness field along the rays. Simultaneously, for each node of the inversion grid, traveltime partial derivatives are computed for *P* and *S* slowness fields, hypocentre location and origin time.

Tests have demonstrated that traveltimes obtained with this procedure are less sensitive to the grid spacing used for the wave front traveltime computation (a maximum error of 0.005 s for a grid spacing of 500 m). For example, given a homogeneous velocity model (4000 m s^{-1}) and a cubic cell grid of 500 m, the comparison with analytical traveltimes indicates that traveltimes computed along the ray are affected by an error twice lower than those estimated by the eikonal solver (10^{-4} and 5×10^{-3} s, respectively). Also, giving a vertical gradient velocity model represented by cell sizes, which range between 500 and 20 m, numerical tests have shown that the error on traveltimes increases if the eikonal solver is used, depending on the cell size and the velocity values. On the contrary, traveltimes calculated along the ray are always lower than 5×10^{-3} s. This represents a significant improvement compared with strategies that directly use eikonal traveltimes from large computation grids.

By following the same numerical procedure of Le Meur *et al.* (1997), parameters are inverted all together without using any parameter separation technique, which has the drawback of filling up the inversion matrix (Pavlis & Booker 1980; Spencer & Gubbins 1980). In order to take into account differences between units of parameter categories, a column normalization/scaling of the partial derivative matrix is performed. Because data are differently sensitive to each class of parameters, we first remove influences of parameter units and then we weight each class by experimentally estimated factors. These latter are defined through synthetic tests having our earthquake–station distribution because the weight factors are configuration dependent.

Finally, the scaled and weighted linear system is solved by using the iterative damped squares method LSQR of Paige & Saunders (1982). The iteration limit is set to 5000 internal iterations of LSQR, while the number of inversion steps is set up to a maximum of 20
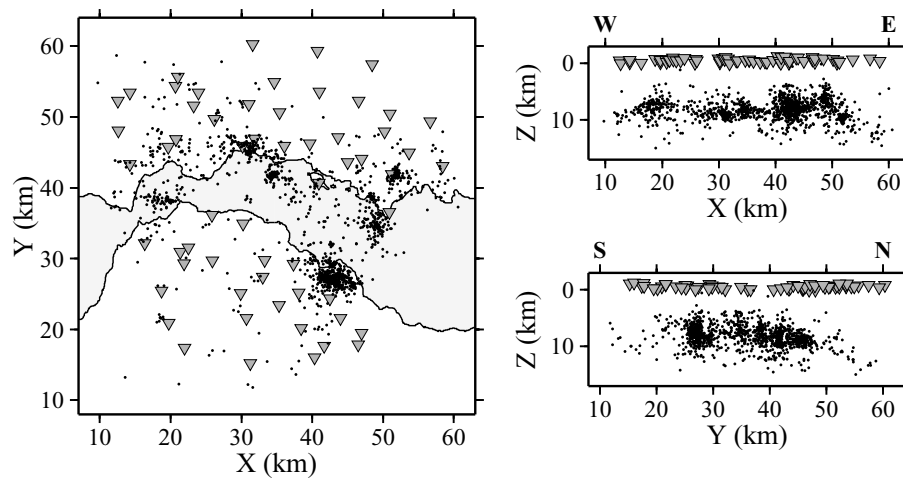
Figure 2. The right panel shows the area where the temporary network of seismic stations (inverted triangles) was deployed during the 1991 seismic experiment. Earthquake hypocentres (dark dots) have been located using the HYPO71 procedure. Right panels show the W–E (top) and S–N (bottom) cross-sections of the investigated area. Earthquakes and stations are projected on these sections.

iterations. Indeed, ray tracing is performed at each step within the new updated velocity structure making the procedure a linearized inversion scheme. The misfit function, defined as the sum of the squared time delays, is *a posteriori* analysed and the convergence is usually reached after 10 or 15 iterations.

4   DATA

The selected area for the tomographic inversion is localized in the western part of the Gulf of Corinth and extends over 56×56 km^2 around the Aigion and the Patras town (Fig. 2).

Our initial data set is composed of 17 722 *P* and 12 906 *S* first-arrival time readings, corresponding to 2260 localized events with magnitude M_L lower than 3.0. This data set was recorded in 1991 by a network of 23 one-component and 37 three-component stations deployed during a two-month seismic experiment in the Gulf of Corinth region. Depending on the station type, record sampling rate ranged between 0.016 to 0.008 ms. Also, time picking accuracy was estimated in a range of 0.005–0.06 s for *P* and 0.01–0.1 s for *S* first-arrival times (Rigo *et al.* 1996).

The collected 1991 data set, only partly available for the first tomography of Le Meur *et al.* (1997), has been entirely reprocessed before our tomographic study. A preliminary hypocentre location has been performed using the HYPO71 code (Lee & Lahr 1975) and the multilayer 1-D *P* velocity model of Rigo *et al.* (1996) (Fig. 3). In this phase, we have not considered earthquakes having less than four *P* and four *S* first-arrival time readings. Upon selection, the resulting data set was composed of approximately 1500 events occurring within the 56×56 km^2 area.

Fig. 2 shows both station coverage and earthquake distribution after the preliminary location. Distances are represented in the X–Y coordinate system derived from the Universal Transverse Mercator (UTM) projection (zone 34). For graphic representation, UTM coordinates are shifted with respect to a local origin point, corresponding to longitude = 21.6°E and latitude = 38°N.

The seismicity recorded during the two-month-long seismic experiment globally shows the same characteristic distribution as the seismic activity observed in the last 10 yr (Bernard *et al.* 1997; Hatzfeld *et al.* 2000; Lyon-Caen *et al.* 2004). Earthquakes spread down to 15 km depth and are particularly concentrated at 6–9 km
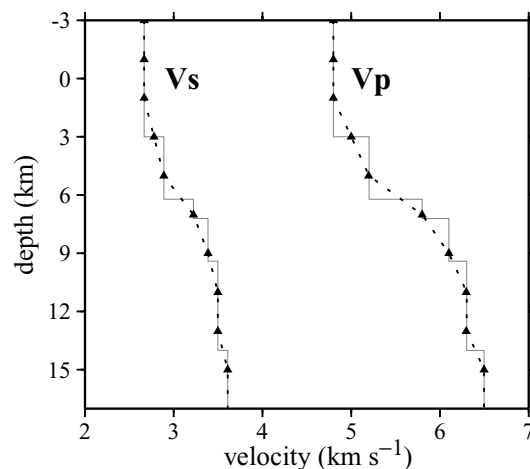

Figure 3. Initial 1-D *P* and *S* velocity models selected for tomographic inversion. Continuous lines represent the multilayer 1-D velocity models of Rigo *et al.* (1996). The 1-D *S* velocity model has been obtained using the Vp/Vs ratio of 1.8 suggested by Rigo *et al.* (1996) for the studied area. Triangles and the dotted lines represent the initial 1-D *P* and *S* velocity models that we have deduced for tomographic inversion. After the initial model analysis (see text), we have deduced that a Vp/Vs ratio of 1.77 is the more suitable initial value for our data set.

depth. Seismicity occurs in clusters, the largest of which is localized south of the town of Aigion.

Although microseismicity is very intense, very low seismicity is observed in the first 4 km of the crust. This event distribution may influence our tomographic results and, hence, we expect to have both a better spatial resolution and a higher accuracy in the deeper part of retrieved tomographic models compared with the shallower part.

5   INVERSION STRATEGY

In order to obtain a well-constrained velocity structure, we have performed several inversions by varying the model parametrization grid as well as the starting velocity model. This procedure allows us to separate well-recovered heterogeneities from artefacts or ghost

images, which might depend on the starting velocity model, the grid parametrization and the limited sampling.

5.1 Model parametrization

Model parametrization of the velocity field should be able to delineate, as much as possible, shape and position of heterogeneities. A nodal representation, in which velocity field is reconstructed by a three-dimensional grid, does not assume a specific geometry of heterogeneities (Toomey & Foulger 1989). Nevertheless, node positions control the tomographic inversion solution. Ray coverage, which mainly depends on station/earthquake distribution, limits the size of the inversion grid. Therefore, our choice of the optimal grid mesh has been determined as a function of the acquisition/events geometry.

During the 1991 experiment, stations were densely distributed all around the gulf with an average spacing of 3–6 km (Fig. 2). Nevertheless, no stations were located inside the gulf, reducing thus our acquisition coverage between the southern and the northern coast, whose average distance is approximately 7–8 km. We have tested different grid spacing to find the best compromise between model parametrization, spatial resolution and a reliable representation of the velocity structure. These tests have demonstrated that a horizontal grid distance of 7 km and a vertical grid distance of 2 km are the smallest spacing achievable without introducing any *a priori* smoothing for our present data set. Therefore, we have parametrized the $56 \times 56 \times 20$ km^3 inversion volume by an inversion grid step of $7 \times 7 \times 2$ km^3. The vertical grid spacing of 2 km is smaller than the one (6 km) used by Le Meur *et al.* (1997). Forthcoming resolution tests will illustrate that this vertical discretization is an optimal compromise between resolution and sensitivity.

5.2 Initial model selection

In a linearized tomographic inversion scheme, an inappropriate reference model choice may give rise to artefacts in inversion results (Kissling *et al.* 1994). Many seismotectonic studies of the western Gulf of Corinth have needed a reference 1-D velocity model. The 1991 data set was first analysed by Rigo *et al.* (1996) to study both earthquake hypocentre locations and focal mechanisms. By following a trial and error approach, Rigo *et al.* (1996) defined an optimal multilayer 1-D *P* velocity model (Fig. 3). Afterwards, this model has been successfully used for the seismic tomography of Le Meur *et al.* (1997) and for the event location of different data sets (Hatzfeld *et al.* 1996; Bernard *et al.* 1997; Lyon-Caen *et al.* 2004). For our study, we have derived a smooth 1-D *P* velocity model from the Rigo *et al.* model (Fig. 3). The *S* velocity model, initially deduced with the Vp/Vs ratio of 1.8 proposed by Rigo *et al.* (1996), has too small values for our observed times. Therefore, several Vp/Vs ratios have been investigated in a range between 1.7 and 1.9. Initial data misfit indicates that the Vp/Vs ratio of 1.77 is the most suitable initial value for our data set and, therefore, it has been selected to obtain the initial *S* velocity model.

Our first concern has been the robustness of tomographic results with respect to our choice of the initial velocity model. Therefore, we have performed several numerical tests for assessing that the 1-D initial model deduced from Rigo *et al.* (1996) is accurate enough for leading to a reliable 3-D final model. For such purpose, we have analysed different input models. In these tests, we have considered two extremes values of *P* vertical velocity profiles (2 and 7 km s^{-1}, respectively) and an initial Vp/Vs value ranging between 1.7 and 1.9. Then, we have randomly extracted 300 1-D *P* and *S* velocity models by requiring always a positive local vertical gradient (Fig. 4). All 1-D models have given an initial rms value between 0.144 and 2.45 s, showing an important sampling of the 1-D input model space. Then, we have performed a 3-D tomographic inversion by starting from the initial models randomly sought. This procedure has provided a best rms value of 0.093 s, which is close to the rms of 0.089 s obtained by tomographic inversion of our initial 1-D model.

By selecting 30 3-D best models (10 per cent of the random models), we have estimated their differences with respect to their average velocity model. These differences represent the variability of inversion results with respect to the initial model selection. When the variability of inversion results is low, all input models converge toward similar solutions, giving some confidence in the sampling of the input model space. On the contrary, a high variability indicates a strong dependence of the final result with respect to the initial
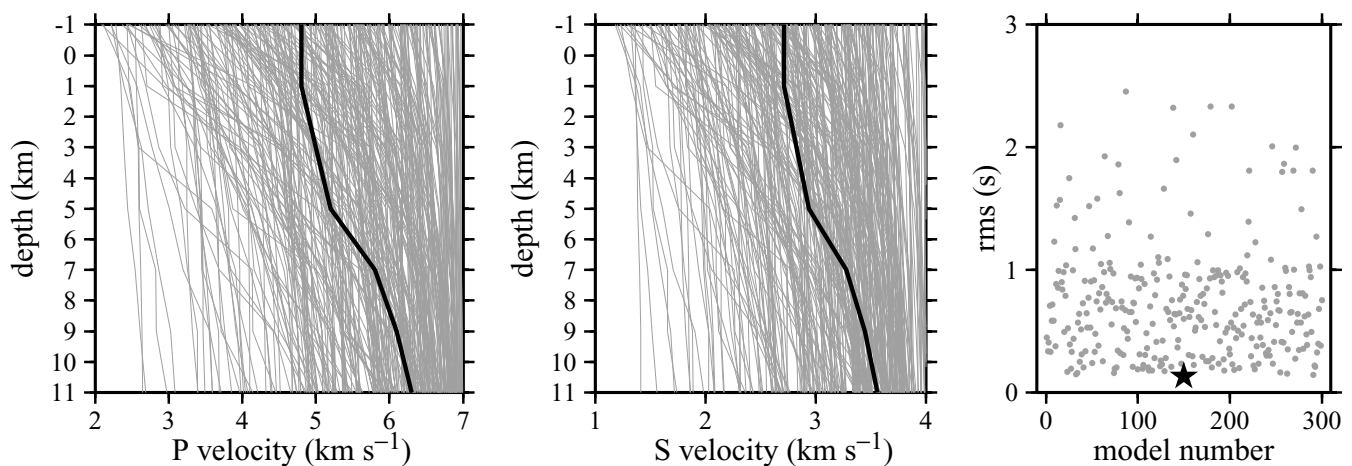

Figure 4. Random sampling of the initial 1-D medium space. (a) By fixing a *P* velocity range between 2 and 7 km s^{-1}, 300 1-D models (grey lines) are randomly extracted. (b) 1-D *S* velocity models are deduced using Vp/Vs values randomly extracted in a range between 1.7 and 1.9. Dark lines represent the reference 1-D velocity models deduced from the 1-D multilayer model of Rigo *et al.* (1996) and using a Vp/Vs ratio of 1.77. (c) Initial data misfits computed for the 300 1-D initial models (grey dots) are shown. The rms values, ranging between 2.45 and 0.144 s, indicate the large sampling of the initial 1-D input model space. The dark star represents the initial rms values of our initial 1-D model selected for the tomographic inversion. This model provides the lowest initial data misfit.

velocity model and we may be far away from the minimum zone of the misfit function. The best 30 inversion models show a variability that decreases from 4–7 per cent in the shallowest part of the models (0–1 km depth) towards 2–3 per cent in the deeper part of the models (7–9 km depth) where we observe a better ray coverage. The estimated variability of the selected 3-D best models is very low considering the large investigation range of the randomly selected velocity models.

Therefore, we may deduce that we have adequately sampled the initial model space for detecting the main minimum zone of the misfit function. Because our selected 1-D model falls into the initial sampling model space and provides both the lowest initial data misfit and lowest final data misfit after 3-D tomographic inversion, we believe that our tomographic results are fairly independent of the initial model we have selected.

5.3 Data selection

Both *P* and *S* first-arrival time picks have been selected using criteria based on their quality and number. By considering the earthquake records shown in Fig. 2, we have selected first-arrival times weighted as a function of their reading quality. Then, after the preliminary earthquake location obtained with the HYPO71 procedure, we have selected picks having traveltime residuals lower than 1.0 s. In order to improve the data quality, we have eliminated all *S* arrival times read on one-component records. Although it significantly reduces the final number of *S* data compared with the *P* data, it improves the global quality of our data set. From this selection, we only consider earthquakes with at least 8 *P* and 4 *S* arrival times readings. Moreover, only earthquakes having rms lower that 0.5 s after the first hypocentre location have been selected. Most of selected earthquakes (more than 90 per cent) present an azimuthal gap smaller than 180°. However, in order to improve the ray coverage at the edge of the network, we have carefully added to the data set events having a gap higher than 180° only when rms values were lower than 0.25 s. Therefore, the final data set used for the tomographic inversion consisted of 12 086 *P* and 4935 *S* first-arrival times, corresponding to 761 earthquakes. Compared with the previous tomographic study of Le Meur *et al.* (1997), we have followed a more severe selection over a significantly larger database. We observe a noticeable improvement of the number of *P* time readings while the number of *S* time readings is slightly fewer in our selection. We believe that this choice allows us to better constrain the *S* velocity structure while keeping the global ray coverage dense enough for a reliable resolution estimation.

5.4 Inversion parameter tuning

Fitting of delay times requires a damping term to obtain physically plausible velocity variations and earthquake distributions. This term removes high-frequency variations, which otherwise would not be constrained during the inversion procedure. When the damping term is large, the new model sets nearby the initial model: the inversion slowly moves towards the final solution by recovering first the low spatial frequency anomalies at the expense of less well fitting delay times.

In order to find the optimal damping value for our data set structure, we have performed synthetic tests using the real station–earthquake configuration and the same model parametrization chosen for the tomographic inversion. Synthetic *P* and *S* velocity models are designed by adding a central positive velocity anomaly within
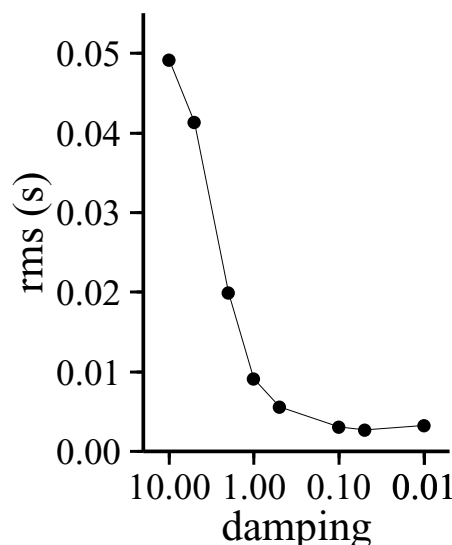

Figure 5. Decrease of rms values for the damping coefficient estimation on a synthetic data set. In the range of damping values between 0.01 and 10, low data misfits are reached for damping values lower than 1.

a homogeneous velocity model. Theoretical traveltimes are computed in these models and are used as observed times. Homogeneous velocity models are considered as initial models and earthquakes are relocated to obtain an initial hypocentre location. For different damping values, in a range from 0.01 to 10, we have inverted simultaneously for both velocity and hypocentre parameters. Test results show that the final rms value is rather high for damping values greater than 1 (Fig. 5). On the contrary, for damping values smaller than 0.1, very low rms values are reached after only three iterations and earthquake locations are well retrieved, showing a maximum error of 160 m. *P* and *S* velocity anomalies are recovered, although images are blurred by artefacts especially on the edges of the model, as expected. Finally, damping values around 0.5 give the best compromise between well-retrieved velocity models and earthquake locations and a rather low data misfit (Fig. 5). By using a damping value of 0.5 in our simple synthetic tests, earthquakes are located with a maximum error of 480 m, which is smaller than the grid spacing size used for traveltime computation. Therefore, we have chosen the damping value of 0.5 as the adapted weighting parameter for the tomographic inversion.

Similarly, in simultaneous inversions of both velocity models and hypocentre parameters, weights chosen for scaling operations between inversion parameters may have a critical influence on the misfit function evolution. Moreover, during the inversion, an adequate weighting allows a similar evolution of very different parameters towards the final solution. Therefore, for our station–events configuration, we made synthetic tests to estimate the most suitable weight to allot to each parameter. By following the same procedure as previously described for the damping coefficient estimation, we perform tests by varying parameter weights. We have analysed the relations between weights controlling *P* and *S* velocity models, spatial location and origin time of seismic events by (i) fixing location of sources and inverting velocities, (ii) fixing velocity models and inverting events parameters, and (iii) simultaneously inverting both velocity models and earthquake parameters. From our tests, we have found that a weighting ratio of 1/1.5 between *P* and *S* parameters and a ratio of 1/5 between models and earthquake location parameters allows the best recovering of velocity amplitudes in our
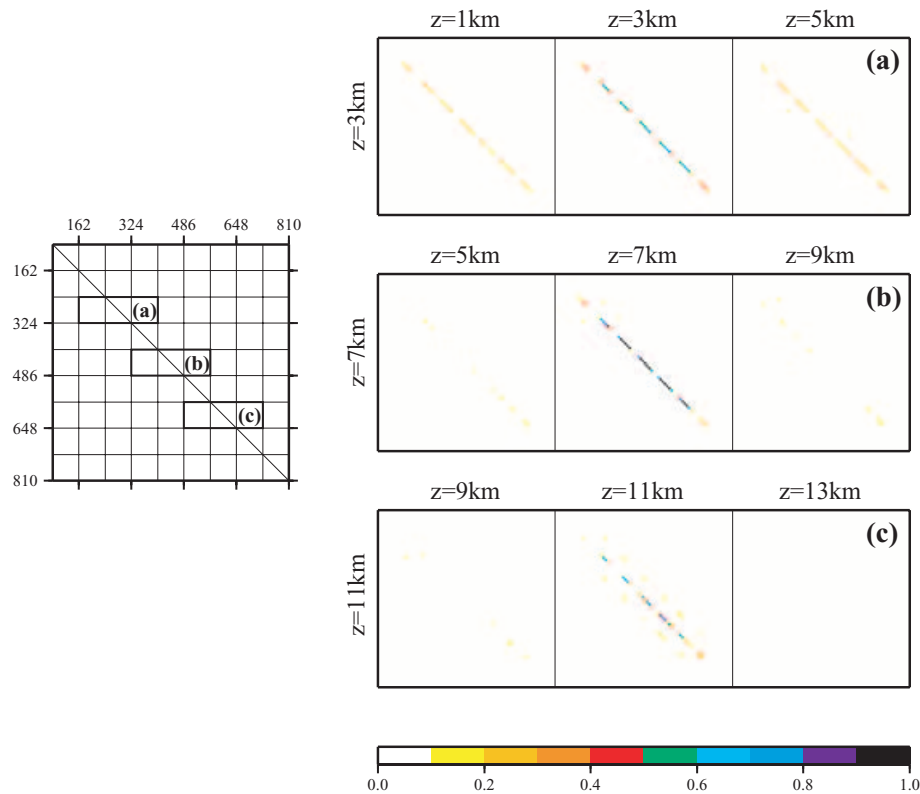
Figure 6. Resolution matrix of the *P* velocity model. Left panel represents the full matrix that we expect to recover. Rectangles a, b and c outline the three enlargements displayed on the right of the figure. (a) Resolution matrix for model parameters located at 3 km depth. The central part of the panel represents the recovered resolution amplitude for elements located at 3 km depth whereas the left and the right part of the figure represent the recovered neighbouring parameters located at 1 and 5 km depth, respectively. Resolution amplitudes are recovered with an observable vertical smearing while no horizontal smearing is detected. (b) Resolution matrix for model parameters located at 7 km depth. Amplitudes are well recovered while both vertical and horizontal smearings are completely negligible. (c) Resolution matrix for model parameters located at 11 km depth. Amplitudes are still recovered for parameters located in the centre of the model but they show a lower resolution power than upper layers and a rather evident horizontal smearing.

station–event configuration. Test results are generally in agreement with the estimated weighting values from Le Meur *et al.* (1997).

6 RESOLUTION MATRIX ESTIMATION

In the framework of the linearized inversion, the resolution matrix estimation must lead to the generalized matrix inversion of the linear system, which relates velocity and earthquake parameters to traveltime data (Menke 1984). The solution of inversion problems by using the LSQR method (Paige & Saunders 1982) does not provide directly the inverse matrix. Therefore, we follow a numerical strategy where spike tests are performed for each parameter of the final tomographic model. For each spike test, the recovery of perturbations for all parameters provides components of the resolution matrix with a possible smearing effect on neighbouring parameters for both velocities and hypocentre locations.

For each spike, we carefully added a velocity perturbation, small enough to prevent noticeable ray distribution variations and strong enough to go beyond numerical noise in traveltime estimation. Synthetic traveltimes are computed in these spike models and, then, are used as input data for the inversion. We have found that good velocity perturbations are equal to 400 m s^{-1} for *P* and 200 m s^{-1} for *S* velocity parameters. We did not perform tests for earthquake locations because of the high number of involved inversions: the resolution matrix is not entirely recovered but the velocity analysis could be achieved in a reasonable amount of numerical tests because spikes have been distributed on internal nodes of our inversion grid,

giving $7 \times 7 \times 9$ *P* spikes and $7 \times 7 \times 9$ *S* spikes, which corresponds to 882 linearized inversions.

Estimated resolution matrix for *P* and *S* velocity parameters are shown in Figs 6 and 7. While we wish a perfect recovery as the identity matrix, the selected depth $z = 3$ km (panel a, Figs 6 and 7) shows an observable but negligible vertical smearing with a partially well-recovered resolution amplitude between 0.5–0.7. On the contrary, no horizontal smearing is detected because of the conservative choice of the horizontal inversion grid spacing. For depths between $z = 5$ km and $z = 9$ km (panel b, Figs 6 and 7), the vertical smearing is completely negligible as well as the horizontal smearing with a good resolution recovery of 0.8–0.9 amplitude for both *P* and *S* velocity parameters. Finer grid spacing would have been possible in this zone if one could better constrain the upper part of the model using active seismic investigations. For depth $z = 11$ km, results show that we can still extract information with a quite limited resolution in the central part of the model. Therefore, we verify that the horizontal grid spacing of 7 km is justified as well as the 2 km vertical spacing.

Another quantification is given by diagonal elements displayed in Figs 8(a) and 9(a), while smearing in hypocentre parameters is described by histograms (Figs 8c and 9c). The overall result is a reliable resolution estimation in the centre part of the model between $z = 5$ km and $z = 9$ km. When we perform spike test on *P* velocity model, we recover *S* velocity parameter perturbations at the same nodes where *P* parameters are poorly constrained. A similar argumentation can be given for the *S* velocity model. This
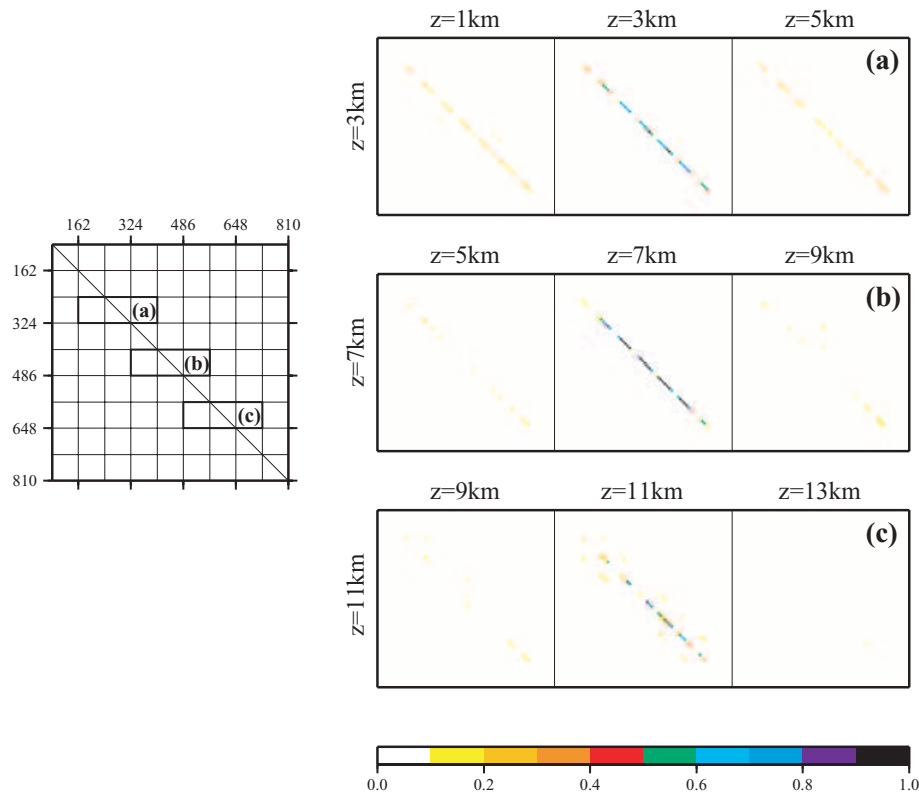
Figure 7. Resolution matrix of the *S* velocity model. Selected areas of the recovered resolution matrix are the same as in Fig. 6.

trade-off between *P* and *S* velocities is shown in Figs 8(b) and 9(b). Fig. 8(b) shows the smearing of the *P* model onto the *S* velocity values. This effect is less evident on the *P* model when we perform spike tests for *S* velocity parameters (Fig. 9b). Because we also invert for hypocentre parameters, spike perturbations can introduce noise in earthquake locations. However, histograms represented in Figs 8 and 9 show that this variation is negligible (lower that ± 10 m). It can be explained with our adequate weighting and scaling between parameters.

In our interpretation of inversion results, we have to take into account limits of the solution quality. We shall analyse only well-recovered parts of velocity models as given by the resolution estimation. Therefore, well-resolved areas of final tomographic results will be outlined using results of the resolution matrix estimation and considering normalized values higher than 0.5.

Checkerboard tests are generally used to describe the degree of smearing of velocity patterns. Moreover, they are often used to estimate the minimum anomaly size that models are able to image correctly. Both smearing degree and minimum resolved anomaly size have been tested for our velocity models. Although checkerboard tests are not necessary because of our resolution analysis, we would like to present one example where a synthetic pattern of $7 \times 7 \times 4$ km anomaly should be recovered (Fig. 10). This illustrated that cautious analysis of checkerboard tests might lead to interesting conclusions. In our checkerboard tests, we add a small anomaly pattern to grid node values of our final velocity models in order to keep the same ray coverage. In Fig. 10, we only display the recovered anomaly pattern in our results. Dark contours outline areas in which the diagonal elements of the resolution matrix have values greater than 0.5. Resolved anomalies are located between 1 and 11 km depth for both *P* and *S* velocity models. The anomaly pattern is not recovered at the surface (first layer) and at 13 km depth. However, strong

lateral smearing is detected at 11 km depth where ray distribution is no able to reconstruct small features. Therefore, we have obtained similar conclusions as the resolution matrix analysis.

7 THREE-DIMENSIONAL *P* AND *S* VELOCITY MODELS AND EARTHQUAKE LOCATION

By inverting the selected data set, final 3-D *P* and *S* velocity structures and earthquake locations are obtained after 15 iterations. From a starting value of 0.132 s, the rms decreases down to 0.089 s. This rms reduction (approximately 32 per cent) represents a noticeable improvement compared with the previous tomographic study of Le Meur *et al.* (1997). For both the *P* and *S* retrieved velocity models, initial and final traveltime residual distributions are displayed in Fig. 11.

Map views of final *P* and *S* velocity models are shown in Fig. 12. Each layer of the figure corresponds to the velocity structure at a selected depth. Only earthquakes located in a range of 1 km around each layer are plotted. The station coverage is presented on the first map view ($z = 0$ km) and main fault positions are indicated on the second layer. Visual correlations are possible over layers for large scale patterns into limits of our spatial resolution. Ray coverage and the diagonal part of the resolution matrix help us to present well-recovered tomographic models. Cells not crossed by any ray have been masked and a contour, corresponding to the 0.5 value of the diagonal part of the resolution matrix, is placed on top of each map view. The following description of velocity models concerns only areas inside this contour.

Reconstructed 3-D *P* and *S* velocity images reveal both strong horizontal and vertical variations. Between 2 and 5 km depths, both high *P* (4.8–5.3 km s^{-1}) and high *S* (2.8–3 km s^{-1}) elongated velocity
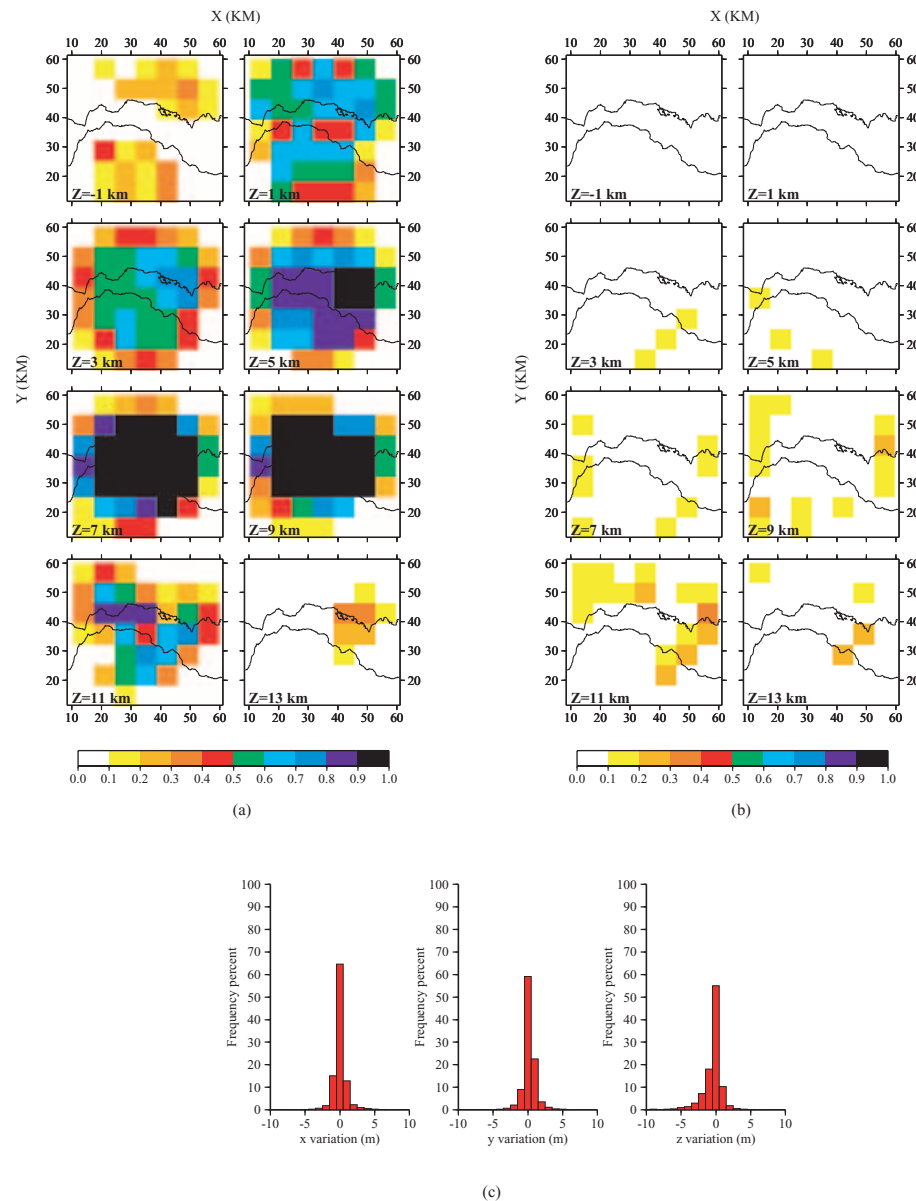
Figure 8. (a) Diagonal part of the resolution matrix for the *P* velocity model. (b) Smearing effects over *S* velocity parameters and (c) hypocentre locations.

structures are located in the northern edge of the gulf, globally following a WNW–ESE direction. While moving from the north to the south, velocity models beneath the gulf show a large-scale low-velocity zone, which follows the graben axis orientation. On land, beneath the northern Peloponnesus, the low-velocity zone extends around the Aigion area, up to the Helike and Pyrgaki–Mamoussia faults, where it reaches minimum *P* and *S* velocities values of 4.4–4.6 and 2.6–2.8 km s^{-1}, respectively. This zone is delimited both westwards and southwards, by similar high velocities observed at the northern edge of the gulf. Both *P* and *S* velocities slowly increase between 2 and 5 km, showing similar large-scale patterns. Seismicity first appears at 4–5 km depth and seems to be especially distributed in the eastern part, between the town of Aigion and the Psaromita peninsula.

Velocity pattern globally changes between 5 and 7 km depths, where a sharp increase of both *P* and *S* velocities occurs (from ∼5.0 to ∼6.2 km s^{-1} for *P* and from ∼3 to ∼3.5 km s^{-1} for *S* average velocity values). In the deeper part (from 7 to 9 km depths) velocity

heterogeneities are characterized by a change in shape and position with respect to the shallower structures. A zone of high *P* velocity (6.2–6.5 km s^{-1}) is located to the north of the Trisonia island at 7 km depth and extends down to 9 km depth at least. Seismicity is mainly located between 7 to 9 km depths. In particular, the northern part of the seismic activity seems to be concentrated at the top of this high *P* velocity zone.

On the contrary, *S* velocity field does not show a large increase at 7 km depth, north of Trisonia or beneath the gulf, while a high-velocity structure appears in the south, beneath the Aigion area. Deeper layers (11–13 km) are also displayed, although seismic activity is weaker in this zone. In the northeastern part of the model, we still note some differences between *P* and *S* velocity features (high *P* and low *S* values), but caution must be taken for these layers because of their poor resolution.

Three SN sections of *P* and *S* velocity models are shown in Figs 13(a) and (b). Their locations are indicated by dotted lines in Fig. 12. N–S sections offer a different point of view, which help to
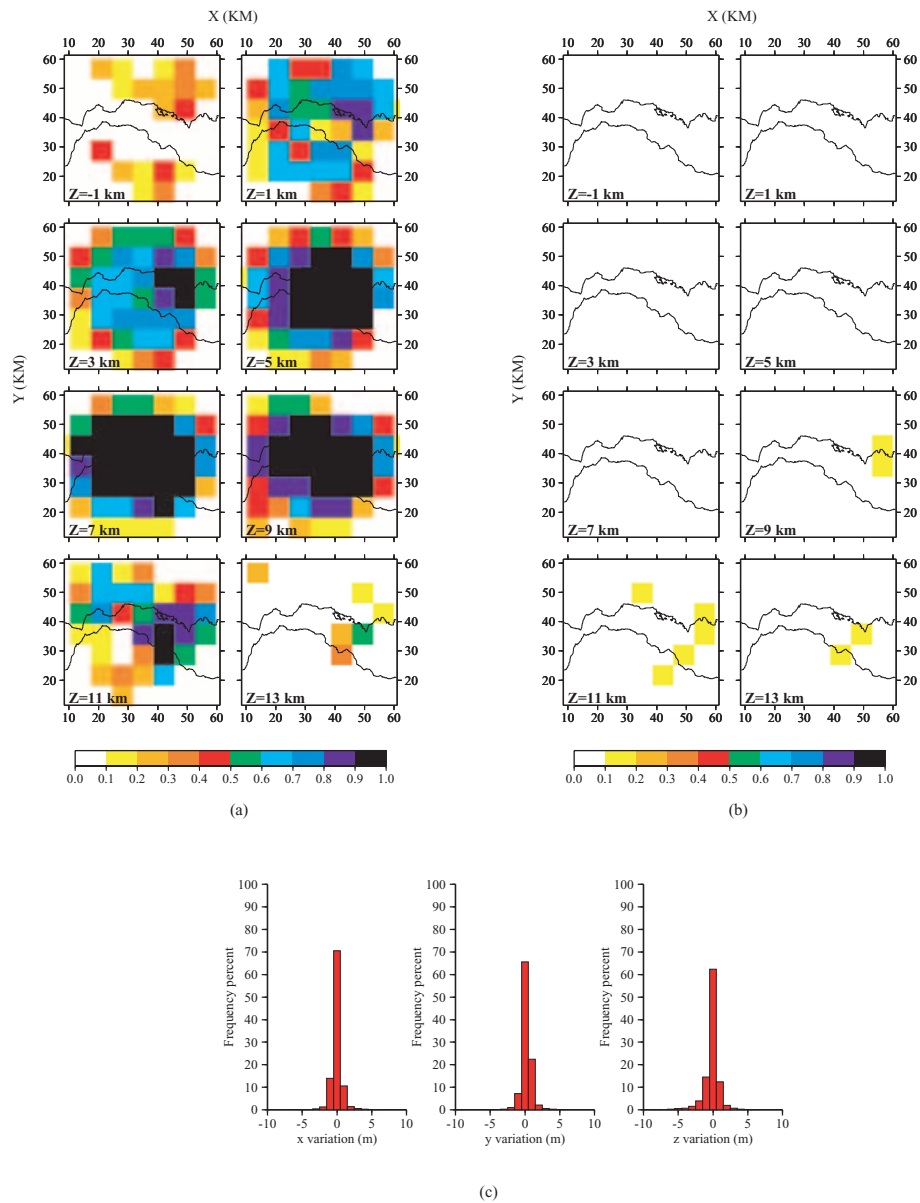
Figure 9. (a) Diagonal part of the resolution matrix for the *S* velocity model. (b) Smearing effects over *S* velocity parameters and (c) hypocentre locations.

highlight the main velocity structures previously described as well as some particular trend of seismicity. For each section, earthquakes located in a 3.5 km wide area around profiles are plotted.

The first section (A1–A2) goes through the Psatophyrgos fault and the western margin of the Helike fault. The low-velocity zone is located below the gulf while northern and southern edges are characterized by both high *P* and *S* velocities. Seismicity is located below 5 km depth and is mainly concentrated in a cluster that lies in the northern part over high *P* velocity zone. In contrast, we have no evidence of *S* velocity increase in this zone.

The second section (B1–B2) displays the central part of the region, to the west of the town of Aigion. The low-velocity zone extends beneath both the gulf and the northern Peloponnesus. This zone is thinner between the Helike and the Pyrgaki–Mamoussia faults (~2 km) while it is thicker beneath the Aigion fault (~4 km). A deeper high-velocity structure is located below the Helike–Aigion area, close to the Aigion cluster. As for the A1–A2 section, northern seismicity is located near a high *P* velocity structure, which does

not correspond to any high *S* velocity feature. Although northern seismicity does not clearly lie over a plane, we can note a general low-angle north-dipping trend of the earthquake distribution.

Trend of the northern seismicity changes in the third section (C1–C2) where event distribution seems to dip with different angles. Moreover, earthquake distribution follows a zone of relatively lower *P* and *S* velocities.

7.1 Comparison with the previous tomographic study of Le Meur *et al.* (1997)

In a previous tomographic study, Le Meur *et al.* (1997) proposed a velocity model of the Aigion–Patras area. Differences existing between the Le Meur *et al.* reconstruction and our own images can be mainly related to differences in the data set and in the grid parametrization. Because of both limited available data sets and grid smooth interpolation using b-splines, Le Meur *et al.* (1997) have selected a vertical grid mesh of 6 km. We have shown that
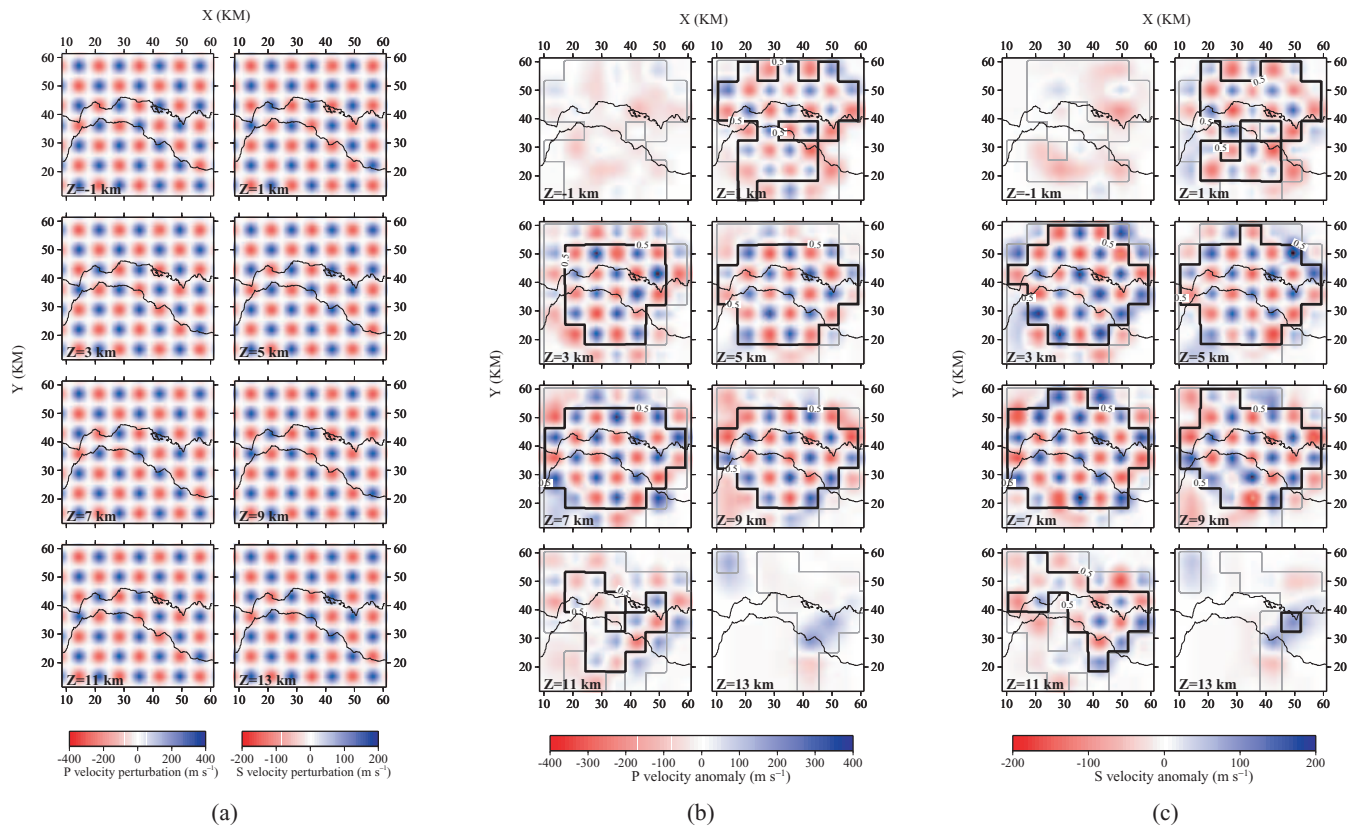
Figure 10. Checkerboard tests for both *P* and *S* velocity models. Synthetic *P* and *S* velocity patterns (a) are added to the 3-D final tomographic models, respectively. The *P* and *S* recovered patterns are displayed in panels (b) and (c). Grey contours represent areas crossed by rays. Dark contours outline areas in which the diagonal elements of the estimated resolution matrix have an amplitude greater than 0.5.
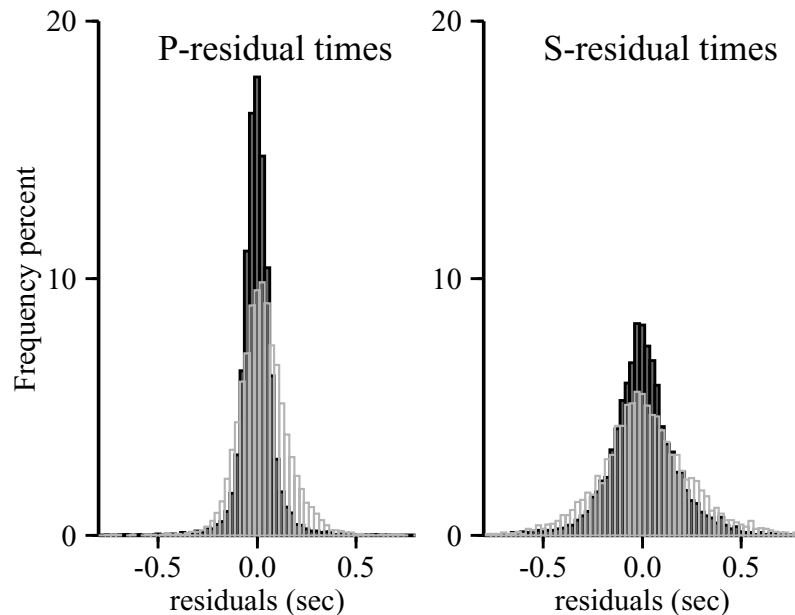

Figure 11. Traveltime residual histograms of *P* and *S* first-arrival times. Residuals before inversion (grey bins) are plotted over those obtained after inversion (black bins).

indeed our data set can reach a much better vertical resolution of around 2 km.

In spite of the mentioned different resolution, large-scale features of our *P*-wave model are similar to the Le Meur *et al.* model such as, for example, the shallower structures or the high *P* velocity body at 9 km depth. On the contrary, other structures, such as the *P* anomalous zone north of Trisonia island, have a different shape and vertical position. Because of our denser grid parametrization, we
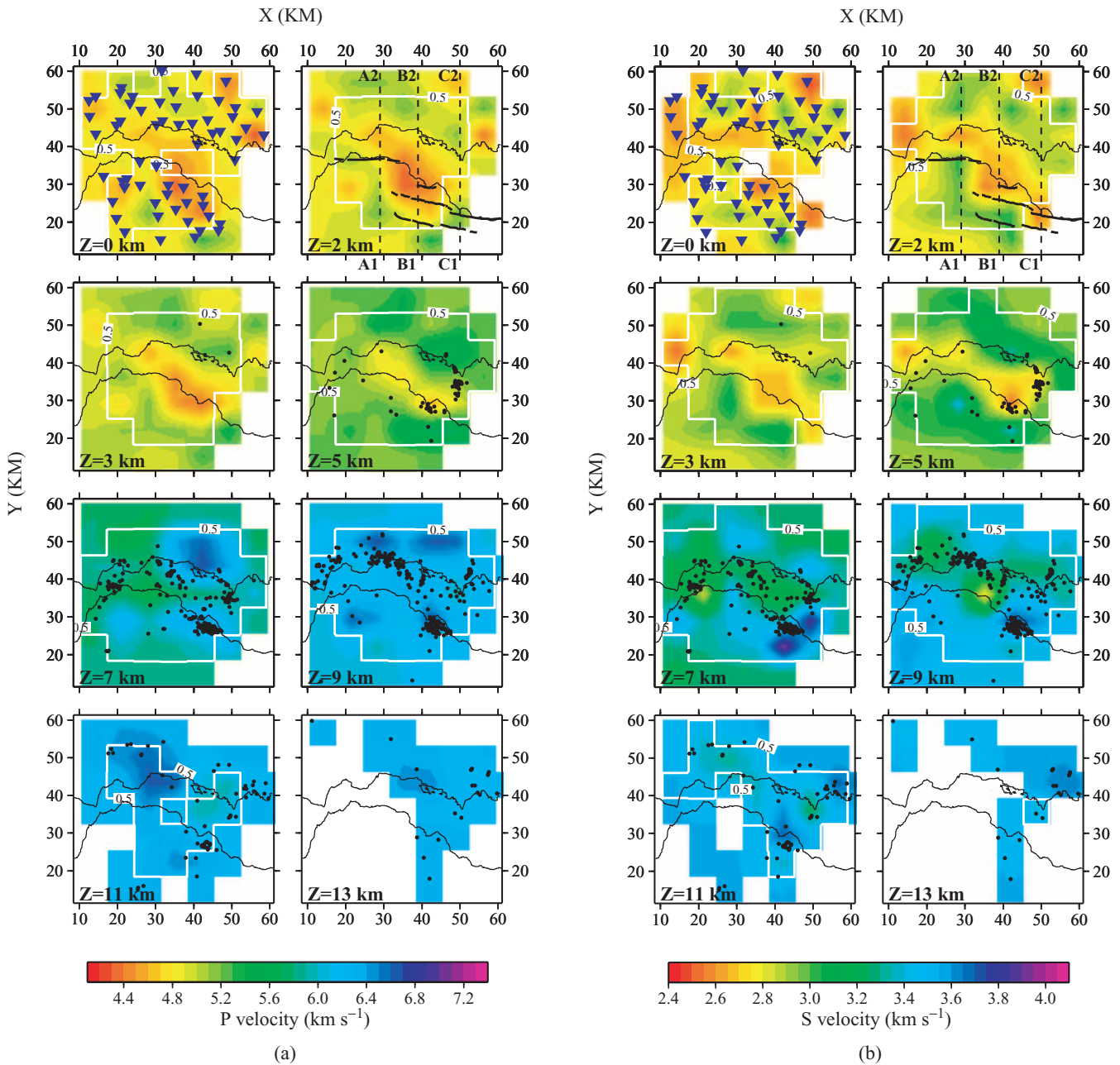
Figure 12. Final tomographic models of (a) *P* velocities and of (b) *S* velocities. Map views show velocity layers between 0 and 13 km depth. Stations are plotted on the first horizontal section. Major normal faults are represented on the second layer (dark lines). Earthquakes located in a range of 1 km around each layer depth are displayed (dark dots). Part of the models not crossed by rays have been masked. Well-resolved areas are outlined with a white contour (see text for more explanations).

can better locate this anomalous zone at 7 km depth. On the other hand, we have found a noticeable difference for the deepest part of the *S* velocity models. This difference is likely to be associated to our more severe data selection. However, resolution tests indicate that our *S* velocity model is well resolved down to 9 km depth and confirms the stability of our results.

More difficult is to compare results relative to earthquake hypocentre locations because of the different data selection. Several earthquakes used by Le Meur *et al.* (1997) have not been considered in our tomography owing either to their location on the edge of the network or the low number of *P* and *S* time readings. On the contrary, several earthquakes have been included in our updated

data set, which was not entirely available for the first tomographic study.

Further interpretations by comparing simultaneously variations of *P* and *S* velocity structures have not been performed by Le Meur *et al.* (1997). Taking into account our higher resolution, we shall proceed in this direction by the analysis of quantities as Vp/Vs and $Vp \cdot Vs$.

8 DEDUCED VP/VS AND $VP \cdot VS$ IMAGES

In seismogenic areas, Vp/Vs anomalies have been often associated with fluid saturation as well as with over-pressured fluid causing
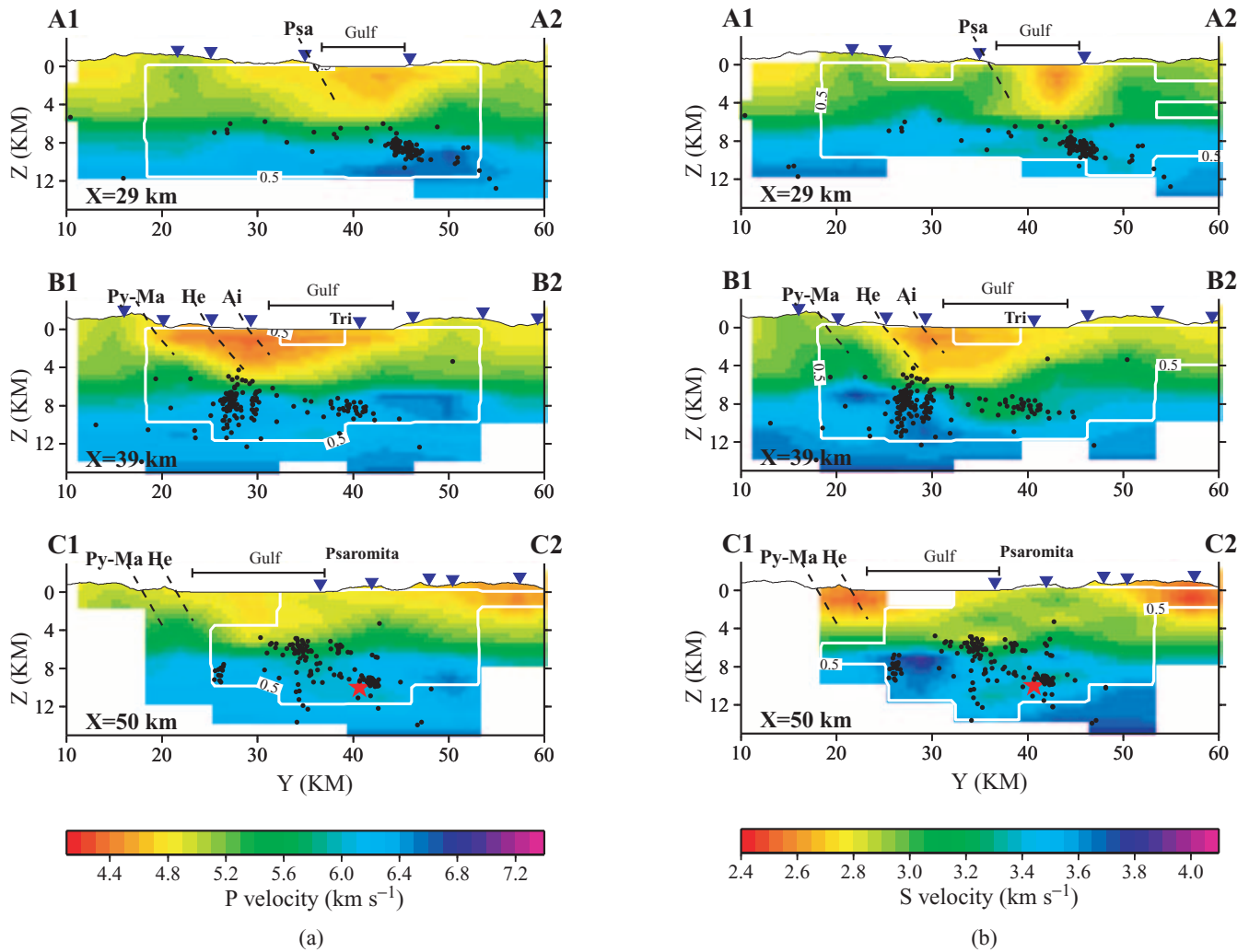
Figure 13. S–N cross-sections of the retrieved (a) *P* velocity model and (b) *S* velocity model. See Fig. 12 for section location. The major normal faults displayed in the sections are: the Psathopyrgos fault (Psa), the Helike fault (He), the Pyrgaki–Mamoussia fault (Py–Ma) and the Aigion fault (Ai). As in the previous figures, velocity models have been masked on the base of the ray coverage and well-resolved areas have been outlined with a white contour.

earthquakes (Zhao *et al.* 1996; Thurber *et al.* 1997; Husen & Kissling 2001; Kayal *et al.* 2002). Because in the active Corinth region a possible relation between seismicity and fluids has been postulated (Rietbrock *et al.* 1996; Bernard *et al.* 1997), we have analysed the spatial distribution of Vp/Vs ratio and of $Vp \cdot Vs$ product to help in discriminating among possible interpretations.

Seismic velocities depend on several rock physical properties, which include lithology, porosity, crack geometry other than fluid content, temperature and pressure conditions (O'Connell & Budiansky 1974, 1977; Ito *et al.* 1979; Tatham 1982). Lithology and porosity both affect *P*- and *S*-wave velocities (e.g. Castagna *et al.* 1985). On the contrary, rock fluid saturation affects only the *P*-wave velocity (i.e. slight *S*-wave velocity changes occur only as a result of a density effect; e.g. O'Connell & Budiansky 1977). It turns out that $Vp \cdot Vs$ distribution emphasizes variations as a result of either lithology or porosity/crack content and so, it minimizes variations related to fluid saturation. On the contrary, the Vp/Vs ratio is more controlled by rock fluid saturation in rocks.

In the present work, we deduce both Vp/Vs and $Vp \cdot Vs$ images from *Vp* and *Vs* tomography results. In order to assess the good quality of these images, an *a posteriori* test has been carried out by

inverting delayed traveltimes using Vp/Vs ratio and $Vp \cdot Vs$ product as original parameters. We have found that *P* and *S* fields, deduced from the inverted Vp/Vs and $Vp \cdot Vs$ parameters, are very similar to *P* and *S* velocity models coming from inversion of delayed traveltimes. It illustrates that indeed for both the *P* and *S* velocity model spaces on the one hand, and for both the Vp/Vs and $Vp \cdot Vs$ model spaces on the other; our inversion results are always located in a minimum zone. Therefore, the non-linear relation between these four parameters does not destabilize our inversion procedure.

Map views and N–S vertical cross-sections are shown in Figs 14 and 15 for both Vp/Vs and $Vp \cdot Vs$ distributions, respectively. We used the same representation of *P* and *S* velocity models and, hence, zones not crossed by rays have been masked while well-resolved areas for both *P* and *S* velocity fields have been outlined. Both $Vp \cdot Vs$ and Vp/Vs images highlight significant changes between the shallow (down to 5 km depth) and the deep structures (7–9 km depth). At shallow depth, the $Vp \cdot Vs$ images better delineate the WNW–ESE elongated structures, which were only slightly evident in the *Vp* and *Vs* maps. These structures are represented by alternate low- and high-velocity zones, with the lowest one occurring beneath the gulf. Low $Vp \cdot Vs$ values are also detected in
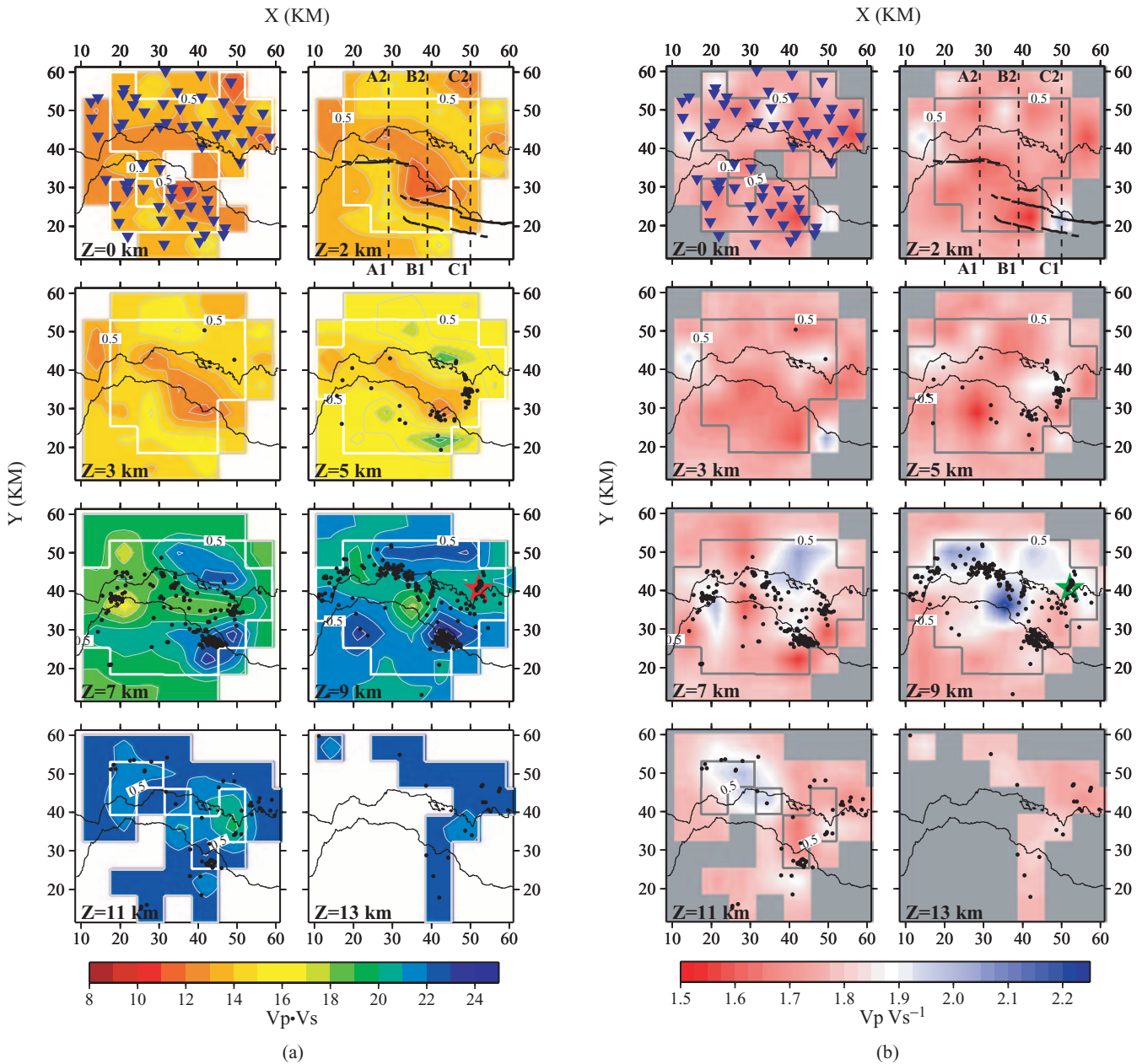
Figure 14. Map views of deduced (a) $Vp \cdot Vs$ product and (b) Vp/Vs ratio. Conventions are similar to Fig. 12.

the Aigion area. On the contrary, the Vp/Vs images do not show relevant anomalies whose values generally range between 1.6 and 1.7. Beyond 5 km depth, two high $Vp \cdot Vs$ zones are located in the eastern part of the area and they spread out as depth increases (9 km depth). A large high Vp/Vs zone ($\geq$1.9) is located at 7 km depth on the north of Trisonia island. As depth increases (9 km depth), the Vp/Vs anomaly extends towards the west and the south, beneath the gulf.

As shown in Figs 14 and 15 the background seismicity is mostly distributed within a lower $Vp \cdot Vs$ area at 7–9 km depth. This seismicity also matches the high Vp/Vs anomalous zone as reported in A1–A2 and B1–B2 sections. Moreover, a variation of seismicity trends is observed going from west to east. The vertical cross-sections of Fig. 15 also report the main directions of fault plane dips as inferred by focal mechanism studies (Rietbrock *et al.* 1996; Rigo *et al.* 1996;

Bernard *et al.* 1997). It is worth noting that earthquake distribution follows the average dip of 15°N (Rigo *et al.* 1996) and of 20°N (Rietbrock *et al.* 1996; A1–A2 and B1–B2 sections, respectively). On the contrary, the earthquake location shown in the C1–C2 section seems to follow a different trend, which results more in agreement to the fault plane dipping 33°N associated with the 1995 Aigion earthquake (green star) (Bernard *et al.* 1997).

9   DISCUSSION

Main velocity features and earthquake locations allow us to distinguish a shallower and a deeper zone in the upper 10–11 km of the crust. The identification of two zones at depth is mainly suggested by (i) the important velocity increase occurring at large scale between
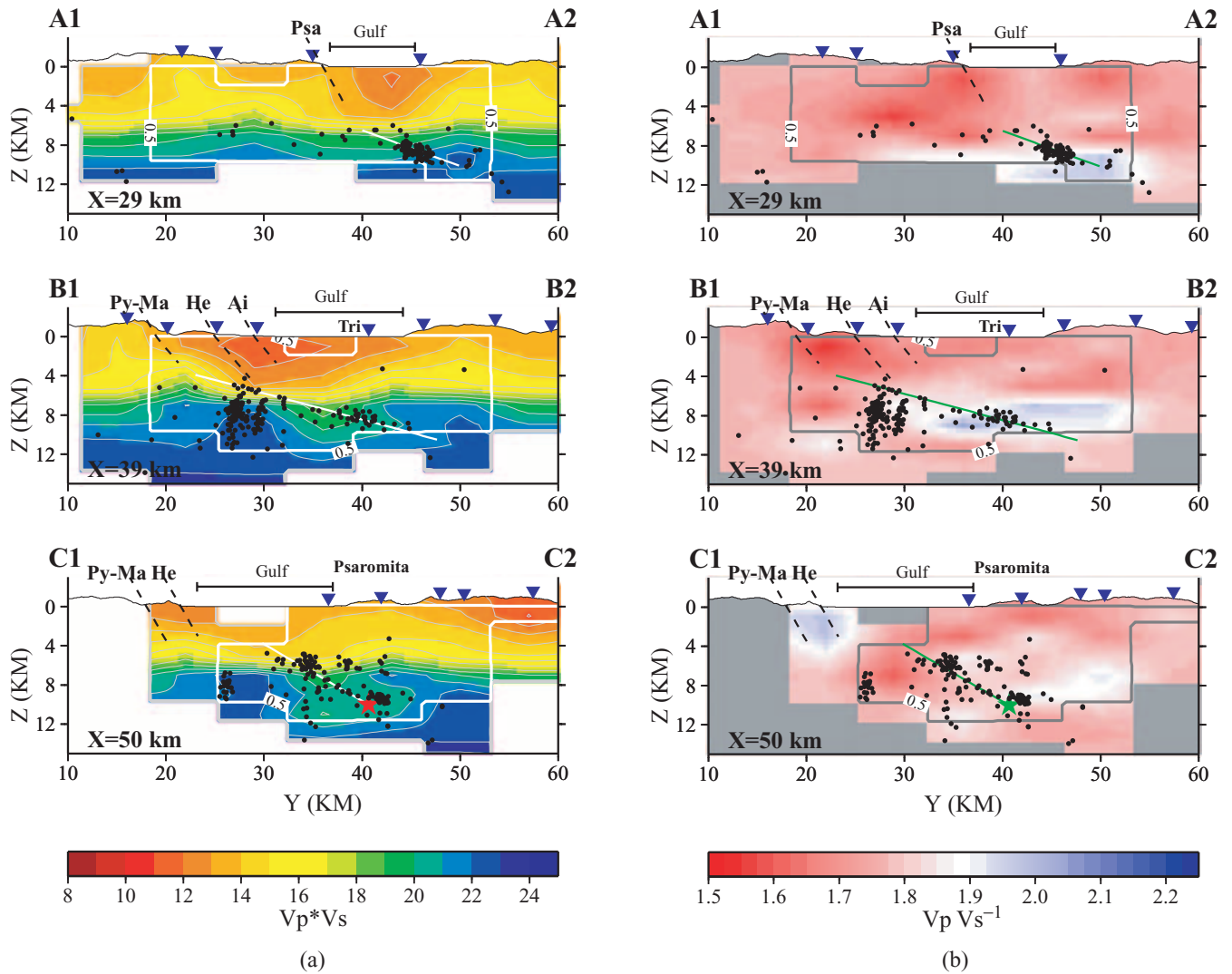
Figure 15. S–N cross-sections of (a) $Vp \cdot Vs$ product and (b) Vp/Vs ratio. See Fig. 14 for section locations. In (a), isolines of $Vp \cdot Vs$ product enhance the increase of both P and S velocities occurring between 5 and 7 km depth. Northern seismicity is concentrated beneath this velocity transition, following a low-angle north-dipping distribution. (b) Main clusters that are located beneath the northern edge of the gulf occur in a large high Vp/Vs zone.

5–7 km depths, (ii) the noticeable change of large-scale velocity patterns, (iii) the anomalous zone of Vp/Vs at 7–9 km depth and (iv) the different seismicity pattern.

9.1 The shallower zone

In the shallower crust, the still active extensive regime seems to affect both trends and positions of main velocity features. The alternation of higher and lower WNW–ESE elongated velocity patterns, with the lowest one corresponding to the gulf location, provide a rather clear image of the graben structure. On the southern edge of the gulf, the distribution of low-velocity patterns is likely to be related to the major faults. Although our resolution is not enough to detect sharp variations, N-to-S horizontal velocity variations (Fig. 15a) may suggest that both the Helike (section B1–B2) and the Psatophyrgos faults (section A1–A2) steeply extend down to at least 4–5 km depth. Also, the Helike fault seems to reach the seismicity located at depth beneath the Helike–Aigion area (section B1-B2, Fig. 15a). Although the number of microearthquakes is too small to define a continuous north-dipping alignment, seismicity between

4 and 5 km shows a spread towards the seismicity located to the north, following an average dip of ∼20° (section B1–B2, Fig. 15a). This result is in good agreement with the model, which postulates a continuation of the major north-dipping normal faults down to the seismogenic zone (e.g. Rigo *et al.* 1996).

The spatial distribution of seismic velocities also points out relevant E-to-W velocity variations in north Peloponnesus. The limit between the lower velocity anomaly of the Aigion area and the higher velocity zone located to the south of the Psatophyrgos fault (Fig. 14a) follows the offset between the eastern margin of the Psatophyrgos fault and the western Helike fault. In this area (i.e. the Aigion area), geological field observations (Doutsos & Poulimenos 1992; Flotté & Sorel 2001) indicate the presence of thick synrift deposits (∼1-km-thick alluvial conglomerates), which overlie the Mesozoic carbonates. Also, a magnetotelluric study has provided evidence of a highly fractured crust in the first 3 km (Pham *et al.* 2000). Both synrift deposits and highly fractured carbonates might be responsible for the low P and S velocities, and hence for the low $Vp \cdot Vs$ values reported in this study. Although we cannot seismically resolve the limit between the upper thin synrift sediments and

the lower fractured pre-rift rocks, we suggest that the observed low-velocity anomaly represents at least the seismic evidence of both structures. Thus, the extension of this low-velocity zone down to 3 km depth would be consistent with findings reported by the interpretation of magnetotelluric data (Pham *et al.* 2000). In this picture, the presence of open fractures in the Aigion area would be expected, suggesting that the present fault activity in this area is very intense and permanent in time. Because we have no evidence of similar signatures in the western Peloponnesus, we speculate that the present fault activity is less intense in the Patras area.

The shallower crust is also characterized by a very low seismicity rate with respect to the deeper crust. In accordance with the results coming from long-term monitoring of seismicity (Lyon-Caen *et al.* 2004), we also note that the microseismic activity is almost missing in the first 4 km. Only four events are located between 3 and 4 km depth, two of them close to the Psatophyrgos and the Aigion faults. Therefore, any mechanical extensive modelling of the Corinth Gulf has also to take into account this peculiar feature shown by the microseismicity distribution.

9.2 The seismogenic zone

The sharp increase of seismic velocities at 5–7 km depth occurs at a regional scale (Fig. 15a). This change is particularly emphasized in vertical $Vp \cdot Vs$ profiles associated, for example, with the Psaromita or the Aigion areas (Figs 16a–b). In the latter, the velocity variation seems to be also controlled by the high-velocity body located at ∼7 km depth (Fig. 14a). The sharp velocity increase is visible in other areas, as shown in the Figs 16(c)–(e), even though with less enhanced amplitudes. Both lithology and porosity/crack content may induce $Vp \cdot Vs$ variations. Geological studies estimate the total structural thickness of both the Pindo and the Gavrovo–Tripolitza tectonic units being approximately 4–6 km (Aubouin *et al.* 1962; Doutsos & Poulimenos 1992; Xypolias & Koukouvelas 2001). Beneath these units, the presence of the Phyllite–Quartzite series occurs as it appears in the Chelmos tectonic window (Xypolias & Koukouvelas 2001). Therefore, we argue that the regional velocity change at 5–7 km depth probably corresponds to the tectonic contact between the Gavrovo–Tripolitza and the Phyllite–Quartzite series, and hence to the lithological variation between these two different tectonic units. On the base of the geological findings, we postulate that the sharp velocity increase occurring at 5–7 km depth might be associated with lithological variations instead of a large-scale crack accruement. Because the structure responsible for the aforementioned velocity transition may likely have a complex geometry, we do not exclude that its depth could locally vary. Also, the hypothesis of the position of this tectonic contact at 5–7 km depth seems to be corroborated by the retrieved seismic velocities, which result, on average, in accordance with the Vp, Vs and, Vp/Vs estimations of phyllite rocks coming from seismic refraction studies and laboratory measurements (Christensen & Mooney 1995; Christensen 1996).

The lithological change deriving from the upper stiff Mesozoic carbonates to the deeper Phyllite–Quartzite series also implies a different mechanical behaviour. Under stress, phyllosilicate-rich rocks exhibit a well-developed fabric that has strong preferred orientations. Therefore, these rocks may represent weaker crustal zones which, as a result of their low friction coefficient, can be responsible for long-term low strength of faults (Wintsch *et al.* 1995). The observed high rate of microseismicity does not involve the entire brittle crust but is mostly concentrated at 7–9 km depth. Consequently, this narrow zone does constitute a preferred environment

for a continuous earthquake triggering. The specific characteristics of the Phyllite–Quartzite series, as well as its position at depth, may provide a reliable explanation for the seismicity concentration at 7–9 km depth which, as remarked by Hatzfeld *et al.* (2000), is a peculiar characteristic of the western Gulf of Corinth.

The seismogenic zone presents a rather complex structure (Figs 14a and b). It is interesting to note that the background seismicity at 7–9 km depth is wholly concentrated in a relative low $Vp \cdot Vs$ zone. This zone is surrounded by two high-velocity bodies, which appear at 7 km depth beneath the Aigion and the Trisonia areas and then extend down to 9 km depth. Although we observe that these deep velocity structures have different seismic signatures from the upper Phyllite–Quartzite series, nevertheless we are not able to propose, at this stage, a reliable interpretation because of the poor information coming from geological studies at these depths. A possible correlation between these bodies and the Plattenkalk unit might be considered because of the relative structural position of this unit with respect to the Phyllite–Quartzite series as proposed by several authors (Jacobshagen *et al.* 1978; Doutsos & Poulimenos 1992; Dornsiepen *et al.* 2001). However, the occurrence at depth of the Plattenkalk unit beneath the Gulf of Corinth is not supported by any geophysical knowledge and, hence, this hypothesis should be further verified.

The seismicity located beneath the Aigion area shows different characteristics with respect to the background seismicity of the gulf (section B1–B2, Fig. 15a). The histogram of Fig. 16(a) shows that earthquakes distribute over a larger depth range (5–11 km depth) than seismicity occurring to the north (Fig. 16c–e). Rigo *et al.* (1996) report that the Aigion cluster is probably associated with a seismic crisis that occurred in 1991 July after the $M_L = 4.5$ event. A recent study dealing with the seismic crisis of 2001 (Lyon-Caen *et al.* 2004) shows that this seismicity locates at 5–8 km beneath the He-like fault. This seismic unrest has been related to the reactivation of a NW-dipping structure probably inherited on the past compressional tectonic phase. This information, together with the absence of a clear relation between the 1991 Aigion cluster (section B1–B2, Fig. 15a) and the shallow faults, leads us to hypothesize that a pre-rifting inherited structure might have played a role in this case too. Nevertheless, the validation of this hypothesis requires more accurate hypocentre relocation studies.

The complex image of the seismogenic zone is also evidenced by some high Vp/Vs anomalous zones occurring to the north (Fig. 14b) of the studied region. In Figs 16(c)–(d), vertical Vp/Vs profiles seem to indicate a possible correlation between the observed Vp/Vs anomalies and clusters located beneath the northern edge of the gulf. These anomalies seem to extend over a regional scale, probably implying that their origin is not related to a local phenomenon. Fluid saturation in fractured rocks can explain the high Vp/Vs ratio caused by the increase of P-wave velocities and slight decrease of S-wave velocities (e.g. Winkler & Murphy III 1995). Metamorphic processes involving phyllosilicate rocks may be responsible for the release of structural water by dehydration reactions. Because we have suggested the occurrence of phyllosilicate-rich rocks within the seismogenic zone, the high Vp/Vs might be caused by the aforementioned metamorphic processes.

Clusters associated to the high Vp/Vs zone (Fig. 14b and 16c–d) have been previously analysed by Rietbrock *et al.* (1996) and Rigo *et al.* (1996). These studies, by providing both focal mechanisms and a high precision relative hypocentre location, have pointed out clear evidence of active low-angle normal faults. As a result of the coupled occurrence of fluid-saturated rocks and dense clusters, we suggest that fluids may be an adjunctive factor in reducing the
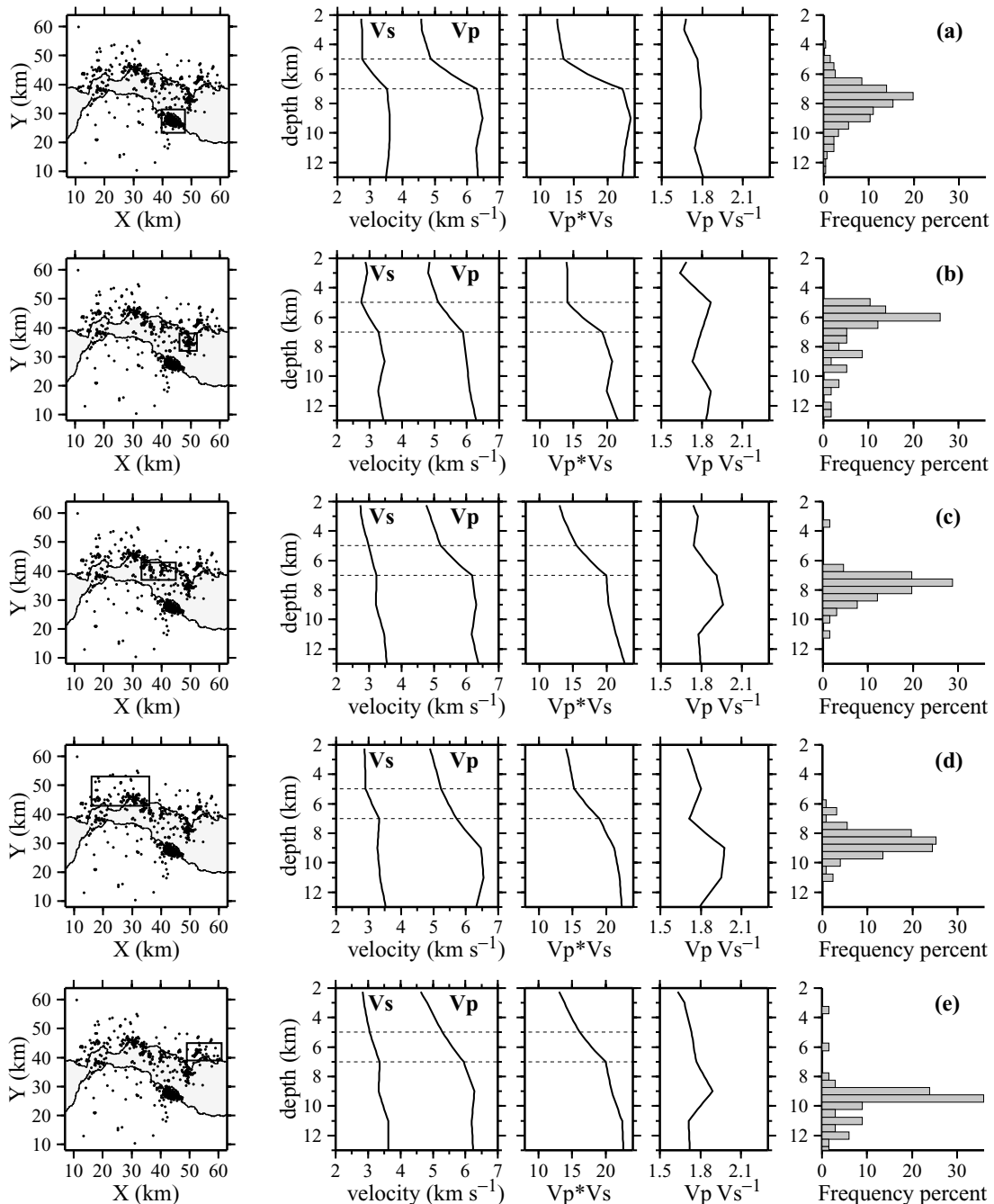
Figure 16. Five representative selected areas (dark box in the maps) are analysed in detail. For points located in the centre of each area, vertical *Vp*, *Vs*, *Vp/Vs* and *Vp · Vs* profiles have been extracted from final 3-D velocity models. Horizontal dashed lines highlight the sharp increase, which affects both the *P* and the *S* velocity models. For these areas, vertical histogram representations of earthquake distribution are also provided. (a) Aigion area, (b) south Psaromita area, (c) north-central area of the gulf, (d) northwestern area and (e) northeastern area. The latter corresponds to the same region in which the 1995 earthquake hypocentre has been located (Bernard *et al.* 1997).

friction coefficient and, therefore, have a possible role in triggering brittle creep along the identified low-angle faults.

10 CONCLUSION

In spite of the intrinsic tomographic resolution limitation, our results have pointed out a quite complex crustal structure. A global very clear feature is the completely different pattern evidenced by the shallow structure on the one hand (0–5 km depth) and the inter-

mediate crust on the other (7–10 km depth). The limit between these two zones occurs at around 5–7 km depth and it is suggested by large-scale sharp vertical velocity increases, by changes in horizontal velocity anomalies distributions and by an increase of the seismicity rate. In the shallow part, the still active extensional regime clearly controls the distribution of the major structures, as evidenced by the main WNW–ESE-trending features of seismic images. Also, the lack of seismicity may be explained by a rather low level of stresses except nearby active faults. On the contrary, the

intermediate crust, which corresponds to the deepest part of our tomographic reconstruction, presents a high seismicity rate. The associated seismogenic zone may be probably related to very specific lithologies of the Hellenic mountain structure (the Phyllite–Quartzite series), which have taken place during the previous compressional phase. Furthermore, fluid-saturated zones may contribute to even increase the seismicity rate and hence to control the stress distribution by a rather horizontally uniform shear zone.

Both inherited structures as well as fluid saturation of key zones may have controlled the present pattern of the microseismicity beneath the western Gulf of Corinth. These elements do improve the present knowledge of the Corinth rift and they should be taken into account in future geodynamical models.

The new tomographic analysis of the 1991 data set has provided us with new insights of the upper crust in the western Gulf of Corinth. Further investigations will require better resolution in the shallower crust between depths of 0 and 4 km, which can be obtained by on-land active seismic explorations. Consequently, the resolution of the intermediate crust image will be improved and one may expect more accurate interpretations.

ACKNOWLEDGMENTS

REFERENCES

Aki, K. & Lee, W., 1976. Determination of three-dimentional velocity anomalies under a seismic array using first P-arrival times from local earthquakes, *J. geophys. Res.,* **81,** 4381–4399.

Armijo, R., Meyer, B., King, G., Rigo, A. & Papanastassiou, D., 1996. Quaternary evolution of the Corinth Rift and its implication for the late Cenozoic evolution of the Aegean, *Geophys. J. Int.,* **126,** 11–53.

Aubouin, J., Brunn, J., Celet, P., Dercourt, J., Godfriaux, I. & Mercier, J., 1962. Esquisse de la géologie de la Gréce, *Mém. Hors Sér. Soc. Géol. France,* **2,** 583–610.

Avallone, A. *et al.,* 2004. Analysis of eleven years of deformation measured by GPS in the Corinth Rift Laboratory area, *C. R. Geoscience,* **336,** 301–311.

Benz, H.M., Chouet, S.A., Dawson, P.B., Lahr, J.C., Page, R.A. & Hole, J.A., 1996. Three-dimentional P and S wave velocity structure of Redoubt Volcano, Alaska, *J. geophys. Res.,* **101,** 8111–8128.

Bernard, P. *et al.,* 1997. The Ms = 6.2, June 15, 1995 Aigion earthquake (Greece): Evidence for a low-angle normal faulting in the Corinth Rift, *J. Seism.,* **1,** 131–150.

Briole, P. *et al.,* 2000. Active deformation of the Corinth rift, Greece: results from repeated Global Positioning System surveys between 1990 and 1995, *J. geophys. Res.,* **105,** 25 605–25 625.

Castagna, J.P., Batzle, M.L. & Eastwood, R.L., 1985. Relationships between compressional-wave and shear-wave velocities in clastic silicate rocks, *Geophysics,* **50,** 571–581.

Christensen, N., 1996. Poisson's ratio and crustal seismology, *J. geophys. Res.,* **101,** 3139–3156.

Christensen, N. & Mooney, W.D., 1995. Seismic velocity structure and composition of the continental crust: a global view, *J. geophys. Res.,* **100,** 9761–9788.

Dornsiepen, U.F., Manutsoglu, E. & Mertmann, D., 2001. Permian-Triassic paleogeography of the external Hellenides, *Palaeogeog. Palaeoclimat. Palaeoecol.,* **172,** 327–338.

Doutsos, T. & Poulimenos, G., 1992. Geometry and kinematics of active faults and their seismotectonic significance in the western Corinth-Patras rift (Greece), *J. struct. Geol.,* **14,** 689–699.

Flotté, N. & Sorel, D., 2001. Structural cross section through the Corinth-Patras detachment fault-system in northern Peloponnesus (Aegean arc, Greece), *Bull. Geol. Soc. Greece,* **XXXIV(1),** 235–241.

Hatzfeld, D. *et al.,* 1996. The Galaxidi earthquake of 18 November, 1992: a possible asperity within the normal fault system of the Gulf of Corinth (Greece), *Bull. seism. Soc. Am.,* **86,** 1987–1991.

Hatzfeld, D., Karakostas, V., Ziazia, M., Kassaras, I., Papadimitriou, E., Makropoulos, K., Voulgaris, N. & Papaioannou, C., 2000. Microseismicity and faulting geometry in the Gulf of Corinth (Greece), *Geophys. J. Int.,* **141,** 438–456.

Hole, J.A., 1992. Nonlinear high-resolution three-dimentional seismic travel time tomography, *J. geophys. Res.,* **97,** 6553–6562.

Husen, S. & Kissling, E., 2001. Postseismic fluid flow after the large subduction earthquake of Antofagasta, Chile, *Geology,* **29,** 847–850.

Ito, H.J., Devilbiss, J. & Nur, A., 1979. Compressional and shear waves in saturated rock during water-steam transition, *J. geophys. Res.,* **84,** 4731–4735.

Iverson, W.P., Fahmy, B.A. & Smithson, S.B., 1989. VpVs from mode-converted P-SV reflections, *Geophysics,* **54,** 843–852.

Jacobshagen, V., Durr, S., Kockel, F., Kopp, K.O., Kowalczyk, G., Berckhemer, H. & Buttner, D., 1978. Structure and Geodynamic Evolution of the Aegean Region, in *Alpes, Apennines, Hellenides,* pp. 537–564, eds Closs, H., Roeder, D. & Schmidt, K.E., Schweizerbart'sche Verlagsbuchhandlung, Stuttgart.

Jolivet, L., 2001. A comparison of geodetic and finite strain pattern in the Aegean, geodynamic implications, *Earth planet. Sci. Lett.,* **187,** 95–104.

Jolivet, L. & Patriat, M., 1999. Ductile extension and formation of the aegean sea, *Geol. Soc. Special Publication,* **156,** 427–458.

Kayal, J.R., Zhao, D., Mishra, O.P., De, R. & Singh, O.P., 2002. The 2001 Bhuj earthquake: Tomographic evidence for fluids at the hypocenter and its applications for rupture nucleation, *Geophys. Res. Lett.,* **29**(24), 2152, doi: 10.1029/2002GL015177.

King, G. C.P. *et al.,* 1985. The evolution of the Gulf of Corinth (Greece): an aftershock study of the 1981 earthquakes, *Geophys. J. R. astr. Soc.,* **80,** 677–693.

Kissling, E., Ellsworth, W.L., Eberhart-Phillips, D. & Kradolfer, U., 1994. Initial reference models in local earthquake tomography, *J. geophys. Res.,* **99,** 19 635–19 646.

Le Meur, H., Virieux, J. & Podvin, P., 1997. Seismic tomography of the Gulf of Corinth: a comparison of methods, *Ann. Geophys.,* **XL,** 1–25.

Le Pichon, X., Chamot-Rooke, N., Lallemant, S., Noomen, R. & Veis, G., 1995. Geodetic determination of the kinematics of the central Greece with respect to Europe: Implicationfor eastern Mediterranean tectonics, *J. geophys. Res.,* **100,** 12 675–12 690.

Lee, W.H.K. & Lahr, J.C., 1975. *Hypo71: a computer program for determining hypocenter, magnitude and first motion pattern of local earthquakes,* Open File Rep.75–311., US Geological Survey, Denver, CO.

Lees, J.M. & Wu, H., 2000. Poisson's ratio and porosity at Coso geotermal area, California, *J. Volc. Geotherm. Res.,* **95,** 157–173.

Lyon-Caen, H., Papadimitriou, P., Deschamps, A., Bernard, P., Makropoulos, K., Pacchiani, F. & Patau, G., 2004. First results of the CRLN seismic array in the western Corinth rift: evidence for old fault reactivation, *C. R. Geoscience,* **336,** 343–351.

Menke, W., 1984. *Geophysical data analysis: discrete inverse theory,* Accademic Press, San Diego.

Mercier, J., Sorel, D. & Simeakis, K., 1987. Changes in the state of stress in the overriding plate of a subduction zone: the Aegean Arc from the Pliocene to the Present, *Annales Tectonicae,* **I,** 20–39.

Monna, S., Filippi, L., Beranzoli, L. & Favali, P., 2003. Rock properties of the upper-Crust in Central Apennines (Italy) derived from high-resolution 3-D tomography, *Geophys. Res. Lett.,* **30,** 1408, doi:10.1029/2002GL016780.

Moretti, I., Sakellariou, D., Lykousis, V. & Micarelli, L., 2003. The Gulf of Corinth: an active half graben?, *J. Geodyn.,* **36,** 323–340.

O'Connell, R. & Budiansky, B., 1974. Seismic velocities in dry and saturated cracked solids, *J. geophys. Res.,* **79,** 5412–5426.

O'Connell, R. & Budiansky, B., 1977. Viscoelastic properties of fluid-saturated cracked colids, *J. geophys. Res.,* **82,** 5719–5735.

Ori, G., 1989. Geologic history of the extensional basin of the Gulf of Corinth (?Miocene–Pleistocene), Greece, *Geology,* **17,** 918–921.

Paige, C.C. & Saunders, M.A., 1982. LSQR: an algorithm for sparse linear equations and sparse least squares, *ACM Trans. Math. Software,* **8,** 43–71.

Pavlis, H.G. & Booker, J.R., 1980. The mixed discrete-continuous inverse problem: Application to the simultaneous determination of earthquake hypocenters and velocity structure, *J. geophys. Res.,* **85,** 4801–4810.

Pham, V.N., Bernard, P., Boyer, D., Chouliaras, G., Mouel, J.L.L. & Stavrakakis, G.N., 2000. Electrical conductivity and crustal structure beneath the central hellenides around the Gulf of Corinth (Greece) and their relationship with the seismotectonics, *Geophys. J. Int.,* **142,** 948–969.

Podvin, P. & Lecomte, I., 1991. Finite difference computation of travel time in very contrasted velocity model: a massively parallel approach and its associated tools, *Geophys. J. Int.,* **105,** 271–284.

Rietbrock, A., Tiberi, C., Scherbaum, F. & Lyon-Caen, H., 1996. Seismic slip on a low angle normal fault in the gulf of Corinth: Evidence from high-resolution cluster analysis of microearthquakes, *Geophys. Res. Lett.,* **23,** 1817–1820.

Rigo, A., Lyon-Caen, H., Armijo, R., Deschamps, A., Hatzfeld, D., Makropoulos, K., Papadimitriou, P. & Kassaras, I., 1996. A microseismic study in the western part of the Gulf of Corinth (Greece): implications for large-scale normal faulting mechanisms., *Geophys. J. Int.,* **126,** 663–688.

Sanders, C.O., Ponko, S.C., Nixon, L.D. & Schwartz, E.A., 1995. Seismological evidence for magmatic and hydrothermal structure in Long Valley caldera from local earthquake attenuation and velocity tomography, *J. geophys. Res.,* **100,** 8311–8326.

Sorel, D., 2000. A Pliocene and still-active detachement fault and the origin of the Corinth-Patras rift, Greece, *Geology,* **28,** 83–86.

Spakman, W. & Nolet, G., 1988. Imaging algorithms, accuracy and resolution, in *Mathematical geophysics,* pp. 155–187, ed. Vlaar, N., D. Reidel Publ. Co., Dordrecht, the Netherlands.

Spencer, C.P. & Gubbins, D., 1980. Traveltime inversion for simultaneous earthquake location and velocity structure determination in laterally varying media, *Geophys. J. R. astr. Soc.,* **63,** 95–116.

Tatham, R.H., 1982. Vp/vs and lithology, *Geophysics,* **47,** 336–344.

Thurber, C.H., 1992. Hypocenter-velocity structure coupling in local earthquake tomography, *Phys. Earth planet. Intr.,* **75,** 55–62.

Thurber, C.H., Roecker, S., Ellsworth, W., Lutter, Y. & Sessions, R., 1997. Two-dimensional seismic image of the San Andreas Fault in the Northern Gabilan Range, central California: Evidence for fluids in fault zone, *Geophys. Res. Lett.,* **24,** 1591–1594.

Tiberi, C., Diament, M., Lyon-Caen, H. & King, T., 2001. Moho topography beneath the Corinth Rift area (Greece) from inversion of gravity data, *Geophys. J. Int.,* **145,** 797–808.

Toomey, D.R. & Foulger, G.R., 1989. Tomographic inversion of local earthquake data from the Hengill-Grensdalur central volcano complex, Iceland, *J. geophys. Res.,* **92,** 17 497–17 510.

Winkler, K. & Murphy III, W., 1995. Acoustic velocity and attenuation in porous rocks, in *Rock physics and phase relations. A Handbook of physical constants,* 3rd edn, pp. 20–34, ed. Ahrens, T.J., American Geophysical Union, Washington, DC.

Wintsch, R.P., Christoffersen, R. & Kronenberg, A., 1995. Fluid-rock reaction weakening in fault zones, *J. geophys. Res.,* **100,** 13 021–13 032.

Xypolias, P. & Koukouvelas, I., 2001. Kinematic vorticity and strain rate patterns associated with ductile extrusion in the Chelmos Shear Zone (External Hellenides, Greece), *Tectonophysics,* **338,** 59–77.

Zhao, D., Kanamori, H. & Negeshi, H., 1996. Tomography of the source area of the 1995 Kobe earthquake: evidence for fluids at the hypocenter?, *Science,* **274,** 1891–1894.